DETECTION OF PROPER MOTIONS IN THE M87 JET

J. A. BIRETTA
Space Telescope Science Institute, 3700 San Martin Drive, Baltimore, MD 21218

F. ZHOU
New Mexico Institute of Mining and Technology, Physics Department, Socorro, NM 87801

AND

F. N. OWEN
National Radio Astronomy Observatory, P.O. Box O, Socorro, NM 87801
Received 1994 September 13; accepted 1994 October 21

ABSTRACT

We present 15 GHz VLA observations of the M87 jet at six epochs spanning 1982 to 1993. Comparison of these images reveals outward motion in five of the brightest knots. Typical apparent speeds are near $0.5c$ (where c is the velocity of light), although knot C near the jet's terminus is significantly slower. Within the knots, individual features often show a large range in speed. Small features within knot D, which is nearest the nucleus, show superluminal speeds up to $2.5c \pm 0.3c$. Motions transverse to the jet axis are also seen. The misalignments between the velocity vectors and jet axis become especially large near the end of the jet where it appears to bend and oscillate from side to side. Constraints derived from the observed motions, as well as the appearance of a sharp edge in knot A, suggest the jet is oriented about $43°$ from the line of sight. We outline a kinematic model for the jet wherein the first kiloparsec consists of a relativistic flow ($\gamma \gtrsim 3$) followed by deceleration in knots A and C. Such a picture can account for important properties of M87 and other F-R I radio sources.

Subject headings: astrometry — galaxies: individual (M87) — galaxies: jets

1. INTRODUCTION

The existence of "jets" or beams carrying energy from the nucleus to the outer regions of extragalactic radio sources was first proposed by Rees (1971) over two decades ago. Since then, many examples of jets have been discovered linking the nuclei to the extended radio structures (Bridle & Perley 1984). Discoveries of super- and subluminal motion in the nuclei of many sources (Porcas 1986) have provided direct evidence for outward flow along these channels. While we expect this flow to continue along the kiloparsec-scale jets and into the extended structures, there is very little direct evidence concerning the velocity of that flow on the kiloparsec scale. In the absence of direct measurements, there have been many efforts to indirectly estimate bulk flow velocities for kiloparsec-scale jets (cf. Bridle & Perley 1984). Arguments based on luminosity and bending typically yield velocities on the order of 10^4 km s^{-1} (e.g., Biretta, Owen, & Hardee 1983, hereafter BOH83; O'Dea 1985; O'Dea & Owen 1987), while a one-sided appearance is often taken as evidence for relativistic beaming and speeds $\sim c$ (Begelman, Blandford, & Rees 1984).

In principle, the same techniques which are used to detect motion in the parsec-scale jets can also be applied to the large-scale jets. By comparing images made a few years apart, it should be possible to directly measure apparent speeds for features in the kiloparsec-scale jets, as is done with VLBI for the parsec-scale jets. An important difference is that the kiloparsec-scale jets have very low surface brightness, so that images with $\gtrsim 0\rlap{.}''1$ resolution must be used. Since the expected position changes are much smaller that this resolution, images with very high dynamic range must be used so that position changes much smaller than the resolution can be reliably measured (Perley 1984). Images with the proper combination of resolution and dynamic range have now been available for

several years. In one of the earliest measurements of this type, Walker, Walker, & Benson (1988) found evidence for motion at $3.7c \pm 1.2c$ in a knot 2 kpc from the core of 3C 120. Later observations set a much lower limit of $< 1.9c$ for motion of this feature, but detected motion at $\sim 3.7c$ in the nuclear jet (Muxlow & Wilkinson 1991). The discrepancy is possibly caused by instability of the core position (Walker 1991). In spite of the discrepancy, these early results hint at the potential of similar measurements for other jets.

A fundamental uncertainty with all proper motion measurements, in both the parsec-scale and kiloparsec-scale jets, is that the apparent pattern speed of visible features in the jet can be different from the bulk flow velocity. Such a situation can naturally arise if shocks are present (Lind & Blandford 1985). But even so, the proper motions can still give a useful indication of the flow speed, especially if several features are seen to move. For example, finding apparent relativistic speeds in many knots in a jet would be fairly convincing evidence for bulk relativistic motion. Alternately, finding the same nonrelativistic speed in all the knots of a jet would be most easily explained by bulk motion near the observed speed.

M87 (Virgo A, NGC 4486, 3C 274) is a giant elliptical galaxy near the center of the Virgo cluster. It contains the closest kiloparsec-scale radio jet in the northern hemisphere, which makes it a prime candidate for proper motion measurements as well as efforts to directly observe a jet's evolution. It is classified as an F-R I radio source (Fanaroff & Riley 1974), and is also a prominent source of optical and X-ray emission (cf. Biretta, Stern, & Harris 1991, hereafter BSH91). Within the nucleus, VLBI observations have obtained a velocity $0.28c \pm 0.08c$ for feature N2 which is located $0\rlap{.}''02$ from the core (Reid et al. 1989). Previous efforts to detect motions in the kiloparsec scale jet gave a velocity of $0.3c \pm 0.2c$ for the bright-

TABLE 1

OBSERVATION LOG

Date	VLA Configuration	Center Frequency (GHz)	Integration Time (hr)	RMS Background Noise in CLEAN Map (μJy beam^{-1})
1982 Mar 4	A	14.435	5	279
1985 Feb 26......	A	14.435, 14.735	10	57
1985 Feb 28......	A	15.035, 15.335	10	65
1989 Jan 15	A	14.435, 14.735	10	64
1989 Feb 5	A	14.435, 14.735	6	85
1989 Apr 10......	B	14.435, 14.735	6	...
1989 Jun 18	C	14.435, 14.735	4	...
1993 Jan 11	A	14.435, 14.735	10	81

est feature, knot A (Biretta, Owen, & Cornwell 1989, hereafter BOC89). These early results also ruled out superluminal motion of several other bright knots. Herein we present new results for M87 which are derived from five epochs of VLA observations with $\sim 0\rlap{.}''15$ resolution spanning 1982 to 1993. Motions outward from the core, as well as transverse to the jet axis, are detected. In addition, superluminal motion is detected within several knots.

Throughout this paper we assume a distance of 16 Mpc to M87 (Mould, Aaronson, & Huchra 1980; Tonry 1991), which gives a linear scale of 78 pc arcsec^{-1}, and motion at 1 mas yr^{-1} corresponds to an apparent velocity 0.254c. Quoted uncertainties represent 1 σ confidence throughout this paper.

2. OBSERVATIONS AND ANALYSES

Observations were made with the VLA[1] in the 2 cm band (Table 1). A 50 MHz bandwidth was observed at each frequency using the continuum correlator. Observations of M87 were made with the phase center positioned south of the jet, at R.A. (1950) = $12^h28^m17\rlap{.}^s000$ and decl. (1950) = $12°40'0\rlap{.}''00$. Observations were also made of a nearby phase calibrator, the flux calibrator 3C 286, and the closure error calibrator 3C 273.

The (u, v, w) coordinates generated by the VLA on-line system were not of sufficient accuracy for our purposes, so they were recomputed from the antenna positions and the recorded time information. At this point corrections were also made for various offsets between the times recorded with the data and the true time of observation. After recomputing the (u, v, w) coordinates, the phase center of each data set was shifted from the observed position to the core component. Precession and nutation cause a slow rotation of the sky about the phase center; these effects were removed by rotating the (u, v) coordinates to their orientation for equinox 1950.0.

2.1. Imaging

After standard calibration of the amplitudes and phases, and editing, the 1985 February 26 data were hybrid-mapped starting with a point-source model. Corrections for closure errors were then derived from the 3C 273 data and applied to the M87 data using the method described by Owen, Hardee, & Cornwell (1989, hereafter OHC89). The data were then self-calibrated, Fourier-transformed, and CLEANed for approximately eight iterations (using ASCAL, UVMAP, and APCLN in the AIPS package) until a final CLEAN image was produced.

The reduction for the other A-array epochs proceeded in a

similar manner, except that CLEAN components from the 1985 February 26 data were used as the starting model for the 1982, 1985 February 28, and 1989 epochs. For the 1993 epoch, the 1989 January 15 CLEAN components were used as the initial model. This initial *cross-calibration* serves to minimize differences in the data sets which might arise from calibration errors. Subsequent iterations of self-calibration should then remove any constraints incorrectly imposed by the cross-calibration. No closure corrections were made for the 1982 data, since its errors were dominated by thermal noise. Other than these differences, the reduction procedures for all epochs were essentially identical.

The final CLEAN images had $0\rlap{.}''10$ resolution and $0\rlap{.}''030$ pixels. The best dynamic ranges (ratio of peak intensity to rms noise; Table 1) are around 40,000:1 for the A-array data. The 1982 data are of poorer quality because of higher receiver temperatures, observation of a single 50 MHz band, and less integration time. The noise is also high for the 1989 February 5 observations because of strong winds, which caused about one-third of the data to be lost, and introduced large amplitude errors for the remaining data. The 1993 data similarly have elevated noise due to clouds and rain.

While the CLEAN images are useful for early stages of self-calibration, the "CLEAN stripe instability" (Cornwell 1983) makes them unsuitable for position measurement by cross-correlation. This instability imposes uniformly spaced parallel ridges of enhanced brightness on regions of extended emission. In our CLEAN images, for example, these ridges have a height of $\sim 10\%$ in the knot A–B region. Because of their uniform spacing and strength, these ridges could introduce significant errors if the CLEAN images were used for position change measurement. Hence, we generated maximum entropy images (Gull & Skilling 1984) for use in the position change measurements.

To make the maximum entropy method (MEM) images we began with the (u, v) data from the final CLEAN mapping. The data were Fourier transformed, and the core region was CLEANed until ~ 2.0 Jy had been removed. This "pre-CLEAN" is necessary since MEM algorithms have difficulty deconvolving extended structure in the presence of a bright point source. The residual image containing the 20″ jet was then deconvolved using MEM (e.g., Narayan & Nityananda 1986, as implemented AIPS task VTESS). During the MEM deconvolution a "default image" [i.e., image $I_0(x, y)$ in the notation of Narayan & Nityananda] was used to provide information about low spatial frequencies which are poorly sampled by the A-array data. This default image was generated using MEM deconvolution on the 1989 B- and C-array data and had a $0\rlap{.}''4$ FWHM resolution. This single default image

was used during deconvolution of all the epochs. In principle this will introduce a small bias forcing the 1982, 1985, and 1993 images to be too similar to the 1989 image, but tests indicate the impact is negligible (see § 2.4). After MEM deconvolution, the core CLEAN components were added back to the deconvolved image, and the resulting image was used to self-calibrate the A-array visibility data. This procedure of self-calibration, Fourier transformation, pre-CLEAN, and MEM deconvolution was repeated for three iterations on each A-array data set.

In making the final MEM images, the pre-CLEANed dirty image was first convolved with a 0″.15 FWHM Gaussian function, and then deconvolved with MEM. This *preconvolution* sets the maximum resolution of the final image, thus preventing superresolution. After MEM deconvolution the CLEAN components from the core were convolved with the same Gaussian function, and added to the image, thus forming the final MEM image. The final MEM images have 0″.15 FWHM resolution, 0″.035 pixels, and cover a field 72″ by 36″ containing the nucleus, the 20″ jet, and most of the bright lobe structure. We did not add the MEM residuals (i.e., the difference between the dirty map and the final MEM image convolved with the dirty beam) to the final image. These residuals appeared to contain only noise together with artifacts near the core from residual closure errors, and we judged that they were unlikely to contribute useful information. Figure 1 (Plates 19–21) shows final MEM maps for epochs 1985 February 26 and 1993 January 11.

Throughout the mapping procedure, and for each epoch, the core components in all images were kept aligned to within 25 μas (0.0007 pixel) of a reference position near the center of a chosen map pixel. This was done by measuring the location of the peak intensity, and then shifting the phases of the (u, v) data so as to move the core to the correct position. We chose to perform these corrections in the (u, v) plane rather than the image plane, so as to avoid image-plane interpolation errors. This method also avoids deconvolution errors caused by different fractional pixel positions of the core (Briggs, Usowicz, & Cornwell 1991). Since the core position tended to drift slightly during self-calibration, its position was measured after each self-calibration iteration, and the phases were adjusted whenever the error exceeded this amount.

2.2. *Measurements of Position Change*

Before measuring position changes, the final MEM images were rotated clockwise 20°.5 to place the jet along the x-axis of the pixel grid. Bicubic Everett interpolation was used during this procedure to place the image on the new pixel grid. This rotation was done merely as a matter of convenience; it introduces minimal error since the resolution is well sampled by the 0″.035 pixels (cf. § 2.4).

Position changes of jet features were measured by computing the two-dimensional cross-correlation of the "unknown" image against the 1985 February 26 image, which served as a reference. We cross-correlated both large regions encompassing entire knots (Fig. 2 [Pl. 22]), and smaller regions encompassing features within knots (Fig. 3 [Pls. 23–25]). For each region of interest, the discrete two-dimensional cross-correlation image $R(\Delta i, \Delta j)$ was computed as

$$R(\Delta i, \Delta j) = \frac{\Sigma_{i,j} I_1(i, j) I_2(i + \Delta i, j + \Delta j)}{[\Sigma_{i,j} I_1^2(i, j) \Sigma_{i,j} I_2^2(i + \Delta i, j + \Delta j)]^{1/2}}, \quad (1)$$

where $I_1(i, j)$ and $I_2(i, j)$ represent the two input images, and Δi

and Δj represent integral pixel shifts in the x- and y-directions, respectively, between the input images. Since the position changes we desire to measure are on the order of a few milliarcseconds, and since it is computationally impractical to make images with such small pixels, we interpolated within the discrete cross-correlation image to find the exact fractional pixel shift between the images, $(\Delta x_0, \Delta y_0)$, which maximized the cross-correlation. This method is feasible since the 0″.15 resolution is well sampled by the 0″.035 pixels. This interpolation was done by fitting an elliptical Gaussian function to a 3×3 grid of pixels centered on the maximum in the cross-correlation image. Such interpolation is exact for a well-sampled image with a Gaussian beam. The height, Δx_0 and Δy_0 position, major and minor axes, and the position angle of the major axis were allowed to vary during fitting. The resulting center of the Gaussian function was taken as the position shift of the feature.

We checked the accuracy of this method by shifting images in the (u, v) plane by known amounts, measuring the shift in the image plane with the cross-correlation method, and then comparing the applied and measured shifts. In one test, we moved the position of the M87 core by shifting (u, v) phases, mapped the data, and measured the core's position change relative to the unshifted data using the cross-correlation method described above. For nine trial shifts covering the range from 0 to 35 mas (0 to 1 pixel), the rms error in the measured position change was 0.0005 pixel or 18 μas. This is a strong test of the cross-correlation method, since the unresolved core has very sharp intensity gradients, which makes it especially susceptible to any errors in the interpolation scheme. Resolved structures in the jet have more gentle intensity gradients, and so would have smaller interpolation errors.

A second test was performed on knot A in the jet. We stretched the (u, v) coordinates (effectively multiplying them by a constant slightly greater than unity), mapped the data, and then measured the position displacement of knot A relative to an unstretched data set using the cross-correlation method. For an applied stretch of 8.75 ± 0.07 mas (0.250 ± 0.002 pixel) at knot A, which approximates its observed motion in 4 yr, the measured displacement was 8.70 mas. This difference between the applied and measured position shift, 0.05 ± 0.07 mas, is consistent with the absence of any systematic error or bias in the cross-correlation procedure. [The uncertainty in the applied shift results from ambiguity in defining the effective centroid of knot A when altering the (u, v) coordinates.] Hence, the cross-correlation technique for measuring position change appears sufficiently accurate for our purposes. The effects of noise and systematic errors on the position change measurement are discussed in §§ 2.3 and 2.4, below.

We note it is important to use a full two-dimensional cross-correlation when measuring proper motions. The one-dimensional cross-correlation (Walker et al. 1988; BOC89; Muxlow & Wilkinson 1991) can give inaccurate results if either the beam or image feature are not circularly symmetric. In these cases the contours of constant cross-correlation are ellipses. If the primary axes of these ellipses are not along the Δx and Δy axes of the pixel grid, then the Δx coordinate of the peak in the one-dimensional cross-correlation $R(\Delta x, 0)$ will be different from that of the full two-dimensional cross-correlation $R(\Delta x, \Delta y)$.

2.3. *Estimation of Random Errors Affecting Position Change*

The largest uncertainties appear to be caused by thermal noise and noiselike defects in the images. These uncertainties

were estimated by a technique similar to that described in BOC89. For each epoch noise images were taken from "empty" regions of the final CLEAN image, multiplied by a correction factor (2.13) and added to the final MEM image of the jet. Then the cross-correlations against the 1985 February 26 reference image were repeated for each jet region. This procedure was repeated for 20 different noise images, and the dispersion in these 20 position shifts for each knot (or region) was taken as the 1 σ uncertainty. The noise images were taken from the CLEAN maps, rather than the MEM images, since the CLEAN images were larger and contained much more off-source area.

The noise multiplier, 2.13, is a correction for the tendency of errors in bright regions to exceed the background noise fluctuations. This value was determined by differencing the two 1985 MEM images, then measuring the rms difference for knots A, B, C, and D, and finally comparing this to the rms difference in nearby regions north of the jet. A similar calculation was made for the pair of 1989 epochs. The resulting eight values of on-source to off-source noise (four knots × two pairs of epochs) spanned a range from 1.81 to 2.50, and had an average value of 2.13, which is the value we adopted.

We have used the 1985 February 26 image as a reference for the cross-correlation, and therefore this epoch is defined to have position zero. Yet errors in this image contribute an uncertainty which has not yet been accounted for. The uncertainty of the 1985 February 26 position was estimated in the same manner as the other epochs, i.e., by adding noise to the 1985 February 26 image, and then cross-correlating it against the 1985 February 26 reference image. This uncertainty was then attached to the 1985 February 26 data point, which by definition has a position change of zero.

These uncertainty estimates may be checked by comparing the position changes seen at near-simultaneous epochs against the uncertainties above. We do not expect to see motions on timescales of a few weeks, so these differences give an indication of the measurement error. Using 18 regions in the jet, we measured the position difference between 1985 February 26 and 1985 February 28, and also the position difference between 1989 January 15 and 1989 February 5. For the 72 position differences (18 regions, 1985 and 1989 data, x- and y-components), the rms position difference in units of the combined uncertainty was 1.16 σ. If the uncertainties were properly estimated, we would expect the rms difference to be 1.0 σ. A possible cause of this discrepancy might be the presence of errors which are correlated over scale sizes larger than the resolution, so that the off-source noise poorly describes the true errors, even after scaling by the above factor of 2.13. To correct this situation, we increased the position uncertainties by 16%, which brought the rms position difference between near-simultaneous epochs to 1.0 σ.

2.4. Estimation of Systematic Effects and Errors on Position Changes

Besides the above random errors, our measurements of position change are affected by several systematic errors. The largest is caused by annual aberration, which produces a geometric stretching in the surface of the sky which varies with time of year. The measured position shifts were corrected for this effect using values of the geocentric velocity tabulated in the Astronomical Almanac. The largest correction for knot A was ~590 μas. The distortion increases with distance from the phase center, so that knots B and C had slightly larger corrections.

Other systematic errors are smaller and so we have not corrected for them. We briefly describe these and estimate the error they are expected to contribute in knot A's position change. In order of decreasing significance, these are as follows:

1. The use of an epoch 1989 default map during MEM deconvolution of the 1982, 1985, and 1993 data causes the position change to be underestimated. Tests indicate the error is about 87 μas in 4 yr.

2. Interpolation errors during rotation of images by 20°.5, $\pm$ ~52 μas.

3. Variations in the effective centroid of the 50 MHz bandwidths between different antennas, which cause errors in the (u, v) coordinates. Study of the closure corrections (i.e., BLCAL results) indicates this error cannot exceed about ~0.2 MHz, which would cause errors in the position of knot A of $\pm$ <40 μas, assuming the error is random among the different antennas.

4. Errors in alignment of cores in different images, $\pm$25 μas.

5. Errors in the (u, v) coordinates caused by asymmetries in the illumination of the antenna apertures. Most parameters of the antenna positions are determined to an accuracy of a $\lesssim$1 mm by measuring interferometer phases for sources distributed around the sky. However, offsets in the plane of the antenna apertures are not measured by this technique. Such offsets are equivalent to a phase gradient across the primary beam patterns of the individual antennas. Since the VLA antenna positions are derived from phase measurements made at a single point in the primary beam, any offsets in the single-dish aperture planes are never measured. The largest offsets are probably caused by errors in aiming the receiver feed horns, which could produce offsets to ~30 cm in the illumination centroids of individual VLA antennas (Napier 1991). Assuming this effect is random among the different antennas, a net error of up to $\pm$ $\lesssim$20 μas could result in the position of knot A. (We note that holographic measurements of the antenna apertures at X-band [$\lambda = 3.6$ cm] on four VLA antennas indicate the illumination centroids are actually much closer to the geometric centers than the above 30 cm estimate, corresponding to errors of a few μas in the position of knot A. It is likely that the 2 cm feed is similar.)

6. Second-order atmospheric propagation delays caused by Earth's curvature (Thompson, Moran, & Swenson 1986), $\pm$ $\lesssim$3 μas.

7. Diurnal aberration, $\pm$ $\lesssim$2 μas.

For a given source and antenna array, the later two effects ([6] and [7], above) depend only on the hour angle distribution of the observations, and so have very little effect, provided the hour angle distributions of the data are similar. The estimates given here incorporate known differences in the hour angle distributions.

Finally, we caution that these observations break new ground in terms of the accuracy of astrometric measurements made within interferometric images. It is possible that some undiscovered error exists which corrupts our results. The reader is reminded of the galaxy rotation curves derived by van Maanen (1916) from proper motion measurements on photographic plates, with the resulting suggestion that the spiral nebulae were galactic phenomena. It is useful to speculate on the nature of any undiscovered errors in the present study. Such an error must affect the 1982 data relative to the 1985 data, and the 1985 data relative to the 1989 data, etc. But it cannot affect the pair of 1985 observations relative to each

TABLE 2

OBSERVED MOTIONS OF ENTIRE KNOTS

Knot	Distance from Core	X Proper Motion[a] (mas yr^{-1})	v_x/c[b]	Y Proper Motion[c] (mas yr^{-1})	v_y/c[d]
D......	3″.3	1.62 ± 0.39	0.41 ± 0.10	0.02 ± 0.14	0.00 ± 0.04
F......	8.5	3.40 ± 0.89	0.86 ± 0.23	-0.53 ± 0.42	-0.13 ± 0.11
A......	12.4	2.01 ± 0.06	0.509 ± 0.015	-0.33 ± 0.09	-0.083 ± 0.023
B......	15.5	2.44 ± 0.20	0.62 ± 0.05	-0.63 ± 0.13	-0.16 ± 0.03
C......	20.3	0.45 ± 0.16	0.11 ± 0.04	0.39 ± 0.18	0.10 ± 0.04

[a] Component of motion parallel to jet axis. Positive values indicate motion away from the core and toward P.A. 290°.5.

[b] Apparent velocity parallel to jet axis in units of c, the velocity of light, for an assumed distance of 16 Mpc.

[c] Component of motion normal to the jet axis, with positive values indicating motion toward P.A. 20°.5.

[d] Apparent velocity normal to jet axis in units of c. Positive values indicate motion toward P.A. 20°.5.

other, or the pair of 1989 observations relative to each other, otherwise it would be detected and accounted for in our uncertainty estimates. Since the data sets are mapped independently (with only an initial cross-calibration), this would appear to rule out imaging problems and concerns about the uniqueness of the final maps. Simple errors in the observing frequency between epochs might have these properties, but such an error would cause position changes which increase with distance from the core, whereas some of the largest motions are observed near the core. Antenna-dependent errors would have the required properties, since they would appear only when the array was reconfigured. The two known errors of this type, namely differences in the 50 MHz IF bandshapes and aperture illumination asymmetries, are discussed above and appear too small to have any effect. In summary, we are unable to identify plausible error sources with the correct properties and magnitude to significantly affect our results. Nonetheless, completely independent measurements (e.g., *HST* observations) would be of great value in confirming the present results.

2.5. *Derivation of Proper Motions from Measured Position Changes*

The position change values measured by the cross-correlation technique, Δx_0 and Δy_0, are plotted as a function of epoch in Figures 4 and 5. These values are relative to the 1985 February 26 position, which is defined as the zero position, since this epoch was used as the cross-correlation reference image. Proper motions were derived by fitting straight lines to these data versus epoch; a least-squares fit was used and the position values were weighted by their uncertainties. The resulting proper motions and corresponding apparent velocities v_x and v_y are given in Tables 2 and 3.

While the proper motions given here are measured on MEM images, we have also made similar measurements on CLEAN images (cf. Biretta & Owen 1990). Results from the CLEAN images are in good agreement with those from the MEM images, though they have a larger scatter about the best-fit proper motion which we attribute to the "CLEAN-stripe

TABLE 3

OBSERVED MOTIONS OF REGIONS WITHIN KNOTS

Knot-Region	Distance from Core	X Proper Motion[a] (mas yr^{-1})	v_x/c[b]	Y Proper Motion[c] (mas yr^{-1})	v_y/c[d]
D-E	2″.7	-0.87 ± 0.45	-0.22 ± 0.12	0.60 ± 0.17	0.15 ± 0.04
D-M	3.3	9.87 ± 1.10	2.51 ± 0.28	-0.11 ± 0.67	-0.03 ± 0.17
D-W	3.8	8.25 ± 0.87	2.10 ± 0.22	-0.91 ± 0.25	-0.23 ± 0.06
A-N	12.6	2.39 ± 0.09	0.607 ± 0.023	-0.38 ± 0.14	-0.10 ± 0.04
A-S	12.6	1.63 ± 0.08	0.414 ± 0.022	0.22 ± 0.18	0.06 ± 0.05
A-E........	12.1	1.88 ± 0.08	0.479 ± 0.019	-0.08 ± 0.12	-0.021 ± 0.029
A-M........	12.6	2.07 ± 0.18	0.52 ± 0.05	-0.86 ± 0.22	-0.22 ± 0.06
A-W........	13.1	2.39 ± 0.26	0.61 ± 0.06	-0.75 ± 0.32	-0.19 ± 0.08
B-NE	14.1	2.07 ± 0.45	0.53 ± 0.11	-0.34 ± 0.31	-0.09 ± 0.08
B-SE	13.8	-0.82 ± 0.75	-0.21 ± 0.19	0.01 ± 0.25	0.00 ± 0.06
B-NM......	14.8	4.93 ± 0.50	1.25 ± 0.13	-0.86 ± 0.31	-0.22 ± 0.08
B-SM	14.5	3.62 ± 0.37	0.92 ± 0.09	-1.41 ± 0.27	-0.36 ± 0.07
B-SW	15.5	2.94 ± 0.49	0.75 ± 0.12	0.48 ± 0.27	0.12 ± 0.07

[a] Component of motion parallel to jet axis. Positive values indicate motion away from the core and toward P.A. 290°.5.

[b] Apparent velocity parallel to jet axis in units of c, the velocity of light, for an assumed distance of 16 Mpc.

[c] Component of motion normal to the jet axis, with positive values indicating motion toward P.A. 20°.5.

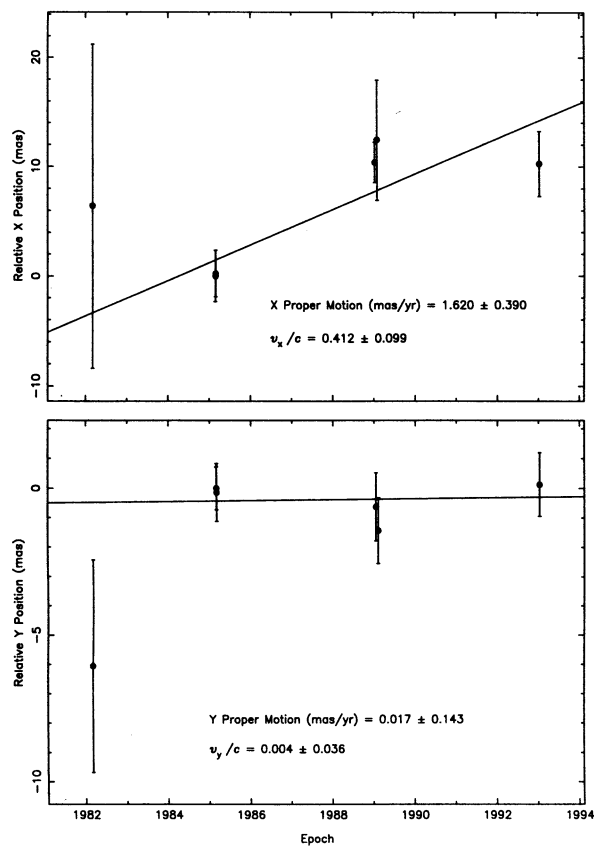[d] Apparent velocity normal to jet axis in units of c. Positive values indicate motion toward P.A. 20°.5.
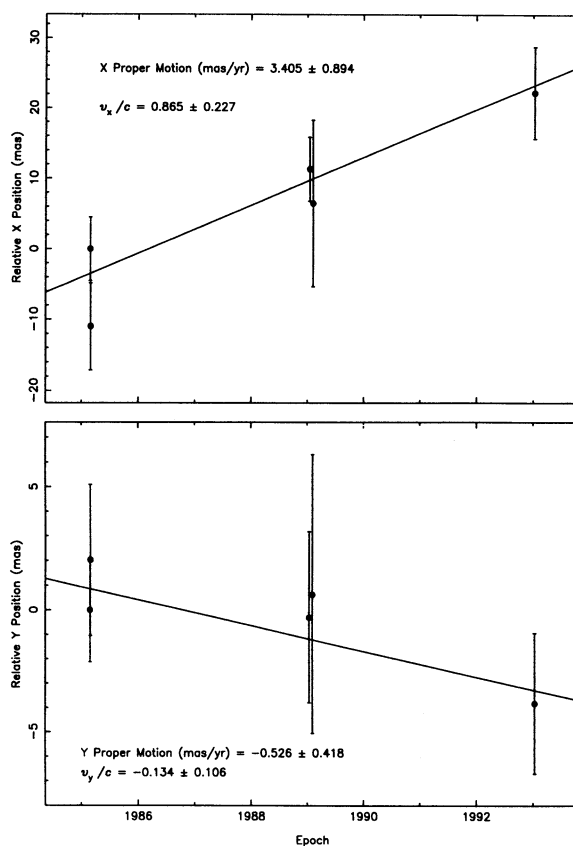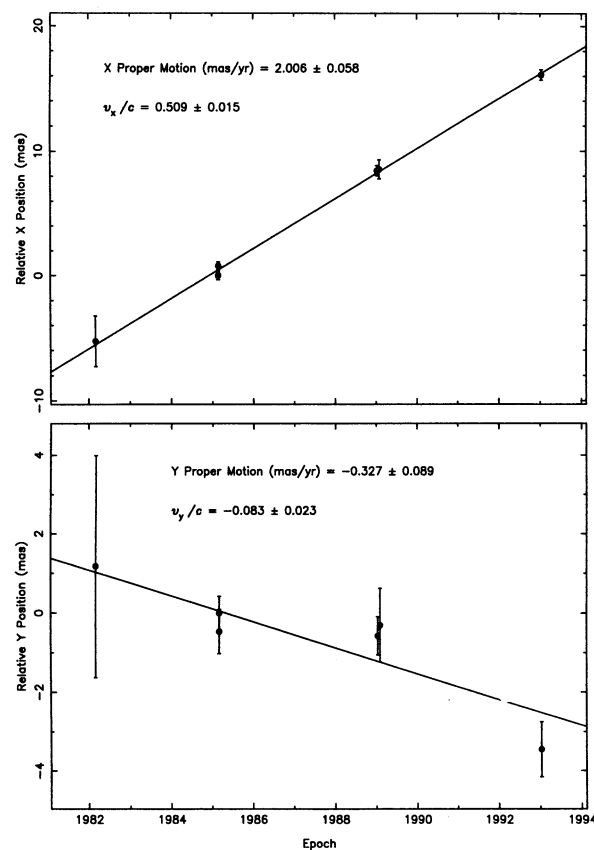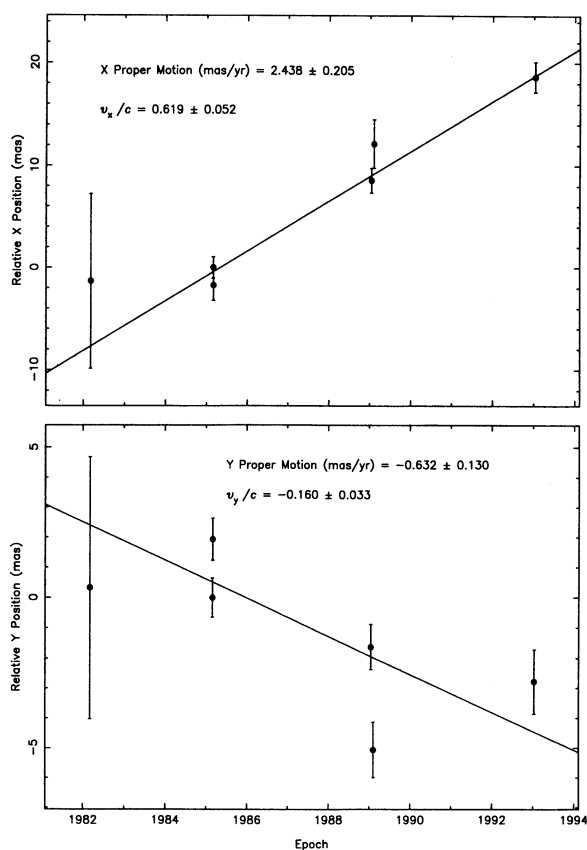
FIG. 4a

FIG. 4b

FIG. 4c

FIG. 4d

FIG. 4.—Observed positions of knots vs. epoch. The top panels show the position relative to 1985 February 26 in the direction parallel to the jet axis (x-component of motion); positive values indicate position displacement away from the core. The bottom panels show the position change normal to the jet axis (y-component of motion), with positive values indicating displacement toward P.A. 20°.5. (a) Knot D. The fitted line in the top panel corresponds to motion away from the core at 1.62 ± 0.39 mas yr^{-1}, or $0.41c \pm 0.10c$. In the bottom panel the fitted line corresponds to motion toward P.A. 20°.5, at 0.02 ± 0.14 mas yr^{-1}, or $0.00c \pm 0.04c$. (b) Knot F. (c) Knot A. (d) Knot B. (e) Knot C.
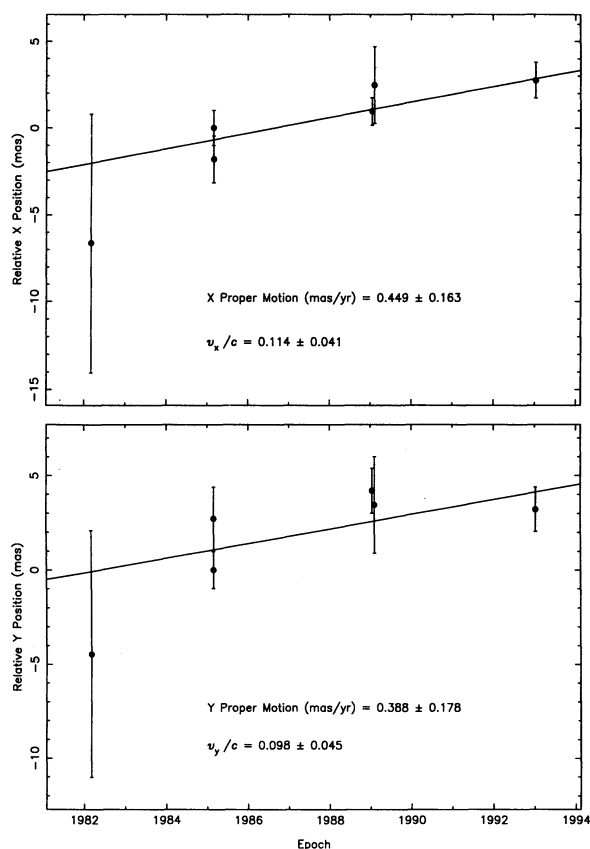
FIG. 4e

instability" described above. We have also observed motions in the jet by visually "blinking" images from different epochs against each other; in all cases the motions seen visually are in qualitative agreement with those found by the more precise cross-correlation measurements.

2.6. Stability of the Core Position

Since our position measurements use the unresolved core component as a point of reference, it is important to consider whether the core position is stable before attributing the position changes to motions within the jet. The following evidence suggests, or is consistent with, the core position being stable:

1. VLBI astrometric observations by Sovers et al. (1988) and Ma et al. (1990), at epochs 1980.0 and 1986.2, respectively, may be used to constrain any long-term motion of the VLBI core relative to other celestial radio sources. After correction for different right ascension zero points used by these groups, we find a motion of the core at 0.3 ± 0.7 mas yr^{-1} toward the northwest. Motion of the core at this speed cannot account for the observed proper motions, which are typically in the range 2–10 mas yr^{-1}.

2. Further evidence against core position change comes from 22 GHz VLBI with submilliarcsecond resolution. While these observations are insensitive to absolute positions, the similarity of the structure seen in 1985 (Spencer & Junor 1986) and 1992–1993 (Junor & Biretta 1995) suggests the core structure, and hence position, is stable.

3. The known motions of VLBI components should have an insignificant effect. For example, the motion of component N2

(Reid et al. 1989), which is located ~ 20 mas from the VLBI core, at 1.3 ± 0.3 mas yr^{-1} would cause the centroid of the VLA core component to move at only $\sim 0.08 \pm 0.04$ mas yr^{-1}. This is estimated from the relative fluxes of the VLBI core and N2, and the spectral indices of these components.

4. The 1982, 1985, 1989, and 1993 axial positions of knot A relative to the core define a smooth, steady expansion (Fig. 4c). This is consistent with the absence of *stochastic* position changes in the core larger than about 1 mas.

The above evidence is consistent with the VLA core position being fixed on the sky. Item (1) rules out uniform motion of the core relative to other radio sources at a rate exceeding about 1 mas yr^{-1}, while items (2), (3), and (4) argue against jitter in the core position exceeding about 1 mas. These limits are smaller than typical motions and position changes we measured in the 20" jet relative to the core. While this evidence is not definitive, it seems reasonable to assume the core position is fixed on the sky and that the observed motions occur solely in the jet; hereinafter we will make this assumption.

Future VLA monitoring of proper motions jet may clarify this issue, if they continue to show an absence of stochastic motions in the jet. In the future, *HST* monitoring of proper motions might allow reference to bright stars and globular clusters within M87, and hence eliminate these uncertainties.

3. RESULTS

Observed proper motions measured on the MEM maps, and their corresponding apparent velocities, are given in Table 2 for five of the brightest knots. We have also made measurements on smaller regions within the knots, and these results are given in Table 3. These motions are all measured relative to the bright, unresolved "core" at the galaxy's nucleus, which we assume to be stationary on the sky. For each region we give two components of the observed motion. The x- or *axial* component of motion is defined as the component parallel to the jet axis, with positive values indicating motion away from the nucleus and toward P.A. 290°.5. The y- or *transverse* component is defined as the component normal to the jet axis, with positive values indicating motion toward P.A. 20°.5. Figures 4 and 5 show the position data from which the tabulated motions were derived. The resulting velocity vectors are illustrated in Figures 6 and 7 (Plates 26–29).

Outward motion is seen in all of the knots bright enough to measure, and in most cases the velocity is a substantial fraction of the speed of light, c. Knot A, the brightest knot, shows the most significant evidence for motion; its apparent axial or x-velocity is $0.509c \pm 0.015c$ outward from the nucleus, for the assumed distance of 16 Mpc (Fig. 4c). Knots D and B show outward motion at roughly similar speeds, $0.41c \pm 0.10c$ and $0.62c \pm 0.05c$, respectively. Knot C near the end of the jet is much slower than the others; its axial speed is only $0.11c \pm 0.04c$ (Fig. 4e). Considering the sizes of the uncertainties it is extremely unlikely that all knots could have the same speed. A simple χ^2 test (Bevington 1969) gives a probability of 1.0×10^{-20} for all knots having the same speed (provided the uncertainties are properly estimated). If we exclude knot C, the probability of single speed increases to 0.048, but is still improbable.

Significant motions transverse to the jet axis (y-component) are indicated in knots A, B, and C (Figs. 4c–4e). There is a trend for velocity vectors to become increasingly misaligned with respect to the jet axis, as distance from the nucleus
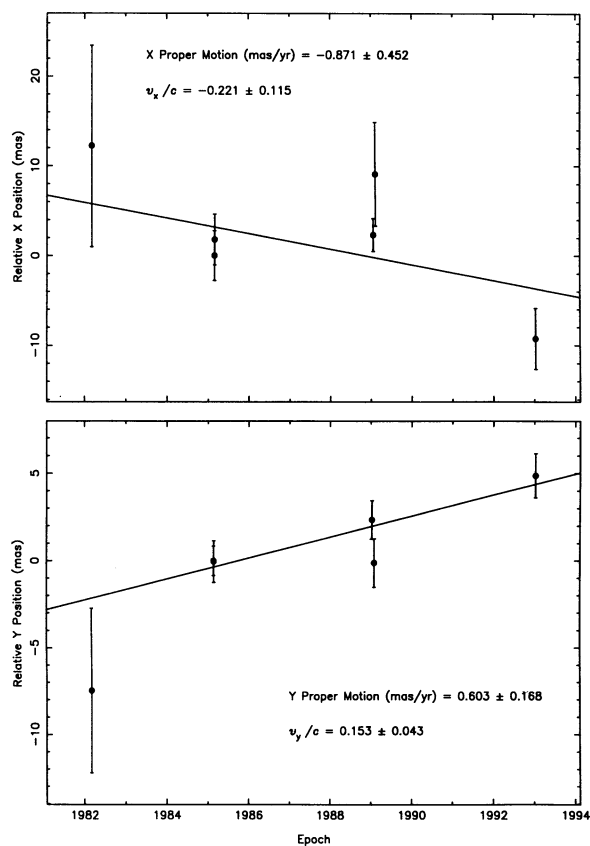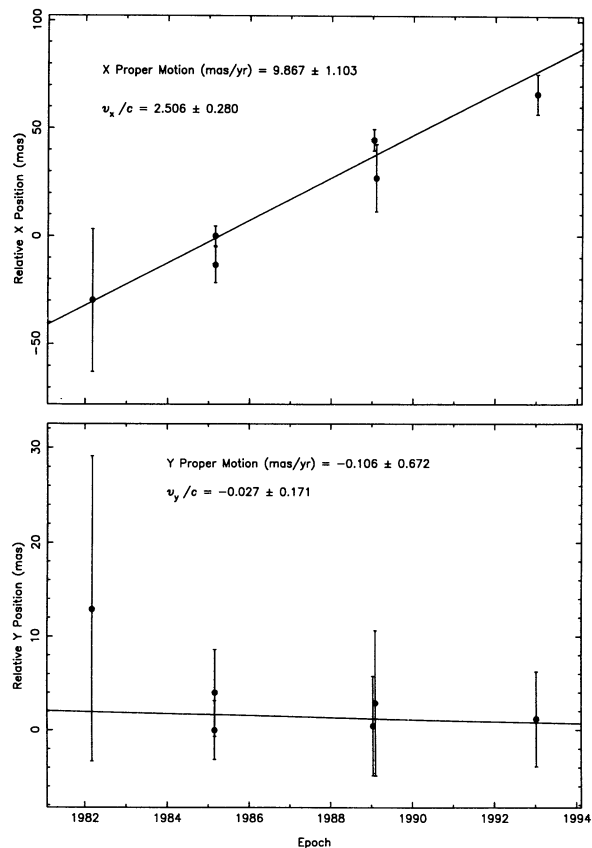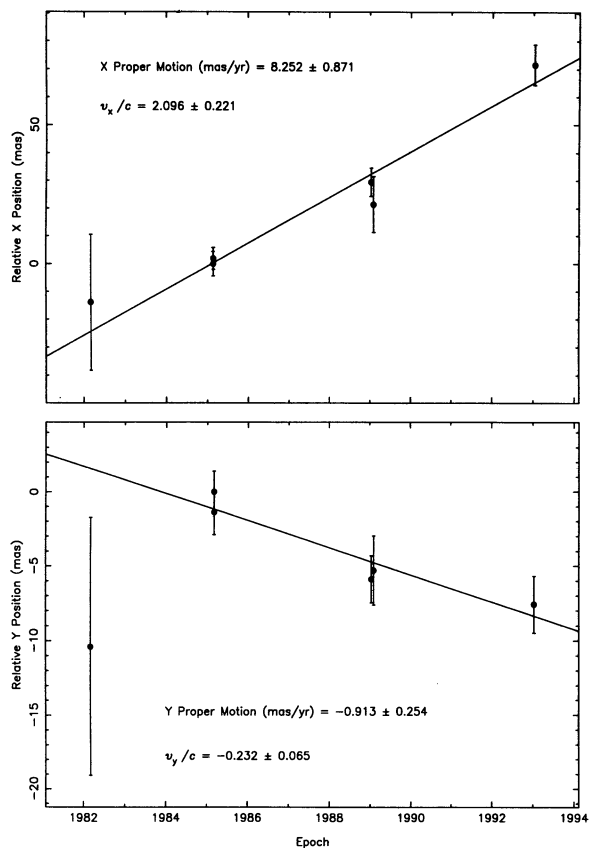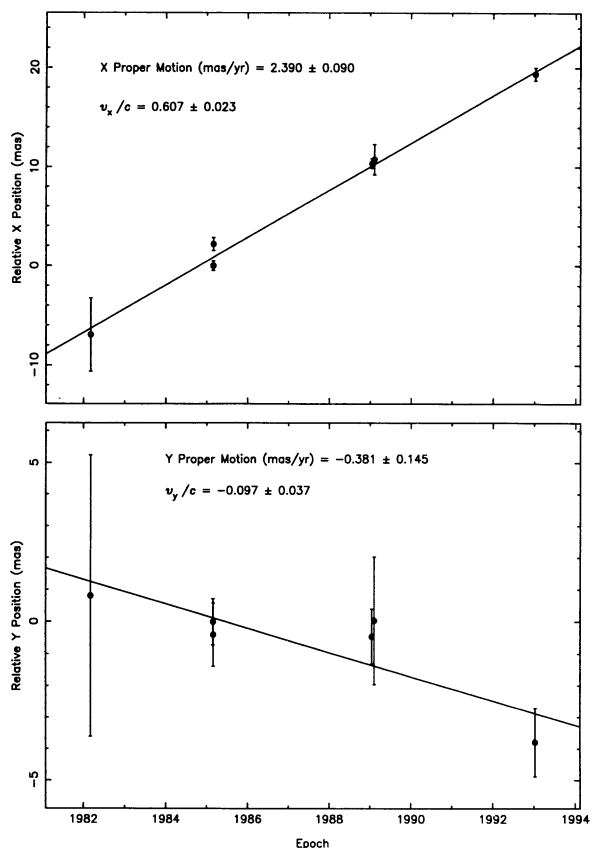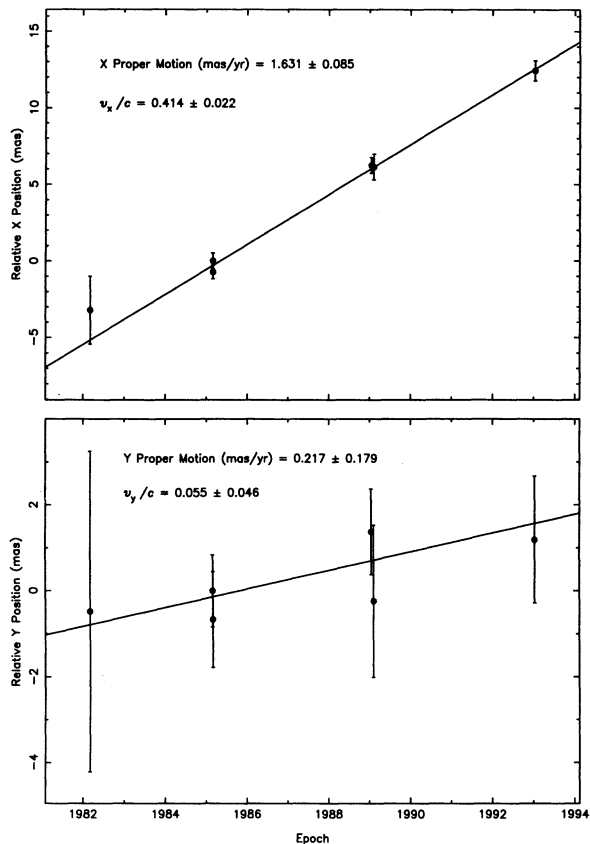
FIG. 5a

FIG. 5b

FIG. 5c

FIG. 5d

FIG. 5.—Representative plots showing position vs. epoch for regions within knots. The top panels show the position relative to 1985 February 26 position in the direction parallel to the jet axis (x-component of motion); positive values indicate position displacement toward P.A. 290°.5. The bottom panels show the relative position normal to the jet axis, with positive values indicating displacement toward P.A. 20°.5 (y-component of motion). (a) Knot D, region E. (b) Knot D, region M. (c) Knot D, region W. (d) Knot A, region N. (e) Knot A, region S. (f) Knot A, region E. (g) Knot B, region SE. (h) Knot B, region NM. (i) Knot B, region SM.
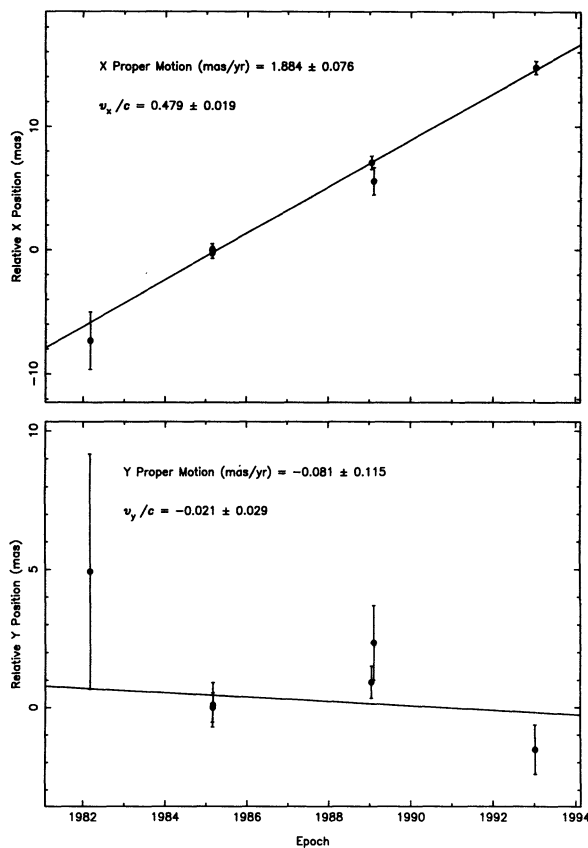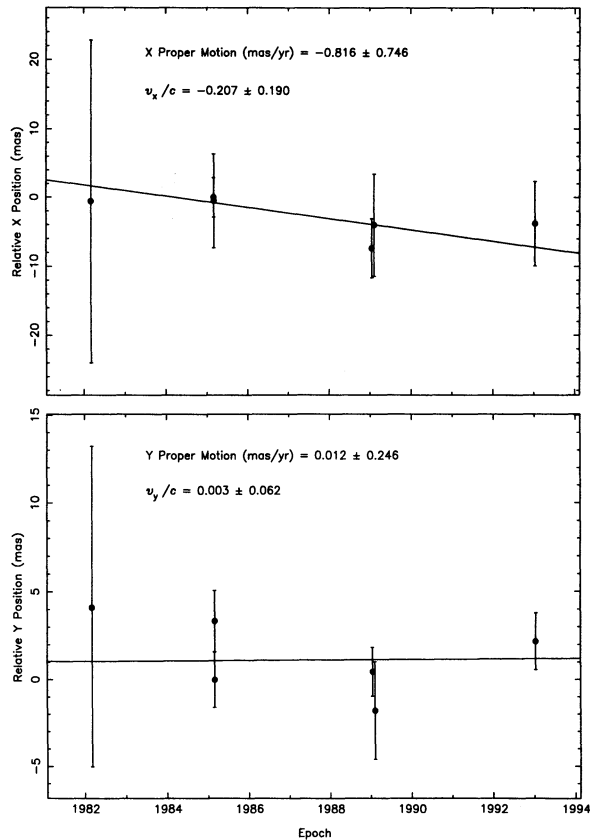
X Proper Motion (mas/yr) = 1.631 ± 0.085

v_x/c = 0.414 ± 0.022

Y Proper Motion (mas/yr) = 0.217 ± 0.179

v_y/c = 0.055 ± 0.046

Fig. 5e

X Proper Motion (mas/yr) = 1.884 ± 0.076

v_x/c = 0.479 ± 0.019

Y Proper Motion (mas/yr) = −0.081 ± 0.115

v_y/c = −0.021 ± 0.029

Fig. 5f

X Proper Motion (mas/yr) = −0.816 ± 0.746

v_x/c = −0.207 ± 0.190

Y Proper Motion (mas/yr) = 0.012 ± 0.246

v_y/c = 0.003 ± 0.062

Fig. 5g

X Proper Motion (mas/yr) = 4.928 ± 0.496

v_x/c = 1.252 ± 0.126

Y Proper Motion (mas/yr) = −0.856 ± 0.313

v_y/c = −0.217 ± 0.080
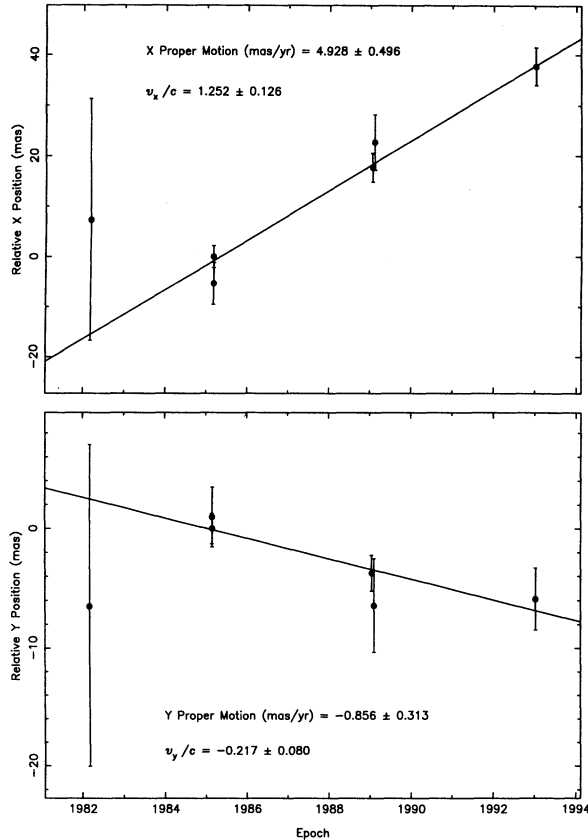
Fig. 5h
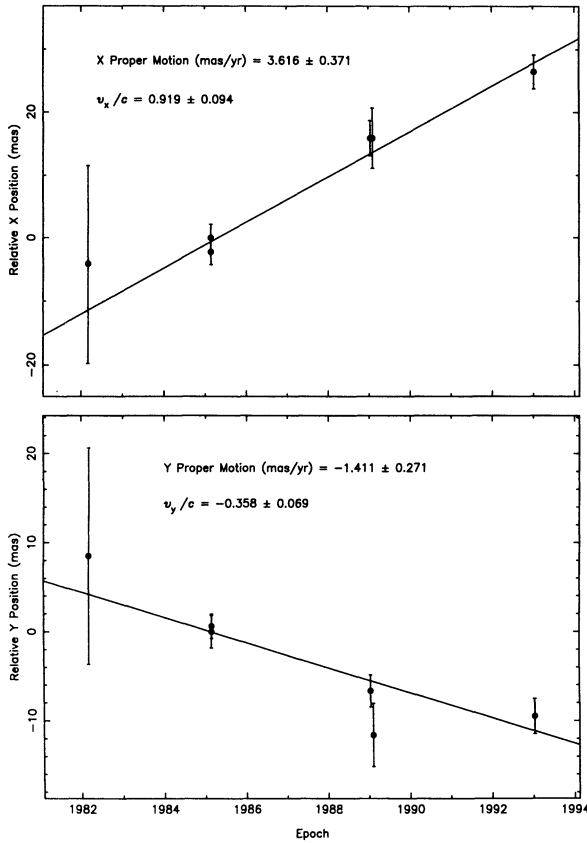
FIG. 5i

increases (Fig. 6). For example, the velocity vector of knot D is directed at $0° \pm 6°$ to the jet axis, whereas that for knot C is directed $42° \pm 12°$ to the jet axis. These misalignments suggest a connection between the velocity field and morphology, which shows increased bending near the end of the jet.

It is interesting to consider whether the knots move as rigid bodies, or whether they possess a wide range of internal speeds. For example, it is possible the emission knots are shocks wherein different pattern and fluid speeds could occur (e.g., Lind & Blandford 1985). Hence we have measured proper motions for smaller features and condensations within the knots. Within knot A we have measured speeds for three distinct features, A-E, A-M, and A-W. Feature A-E is the bright transverse ridge which extends across the jet's width, A-M is a broad condensation near the middle of the knot, and A-W is a weak linear feature which also extends across the jet near the western edge of knot A (Fig. 3b). These regions have a small range in axial speeds with values ranging from $0.48c \pm 0.02c$ to $0.61c \pm 0.06c$. We also divided knot A into northern and southern halves and found that the northern half is moving significantly faster than the southern half ($0.61c \pm 0.02c$ versus $0.41c \pm 0.02c$; Figs 5d and 5e). It appears that the bright ridge in knot A is rotating clockwise on the sky, so as to become more nearly normal to the jet's axis. The range of speeds in knot A is relatively small and is only $\pm 20\%$.

Knots B and D, however, show much larger ranges in their internal speeds. Three different regions in knot D show speeds ranging from $-0.2c$ to $2.5c$. Feature D-M is a small condensation at the middle of the knot near the southern jet limb. It is the fastest feature we measured, with a superluminal speed of

$2.5c \pm 0.3c$ (Fig. 5b). Feature D-W is a broad condensation adjacent to D-M and its speed is similar, $2.1c \pm 0.2c$. In spite of the large axial speeds, these regions have small transverse speeds of $-0.03c \pm 0.17c$ and $-0.23c \pm 0.06c$, respectively. Their velocity vectors point almost directly away from the nucleus (Fig. 7a). The brightest and most compact feature within knot D, feature D-E, stands in sharp contrast to these superluminal regions. It appears to have slow *inward* motion at $-0.22c \pm 0.12c$ or might be stationary, given the uncertainties. As evident in Figure 5a, the inward motion is caused largely by the 1993 epoch; the earlier epochs merely indicate a lack of motion. Given that the morphology of D-E changes by epoch 1993 (Fig. 1), it is conceivable that the inward motion is an artifact of structural change, rather than actual motion towards the nucleus. A χ^2 test gives a very low probability, 4×10^{-31}, of a single speed throughout knot D.

Knot B also shows a large range of internal speeds. Five different regions show axial speeds ranging from $-0.21c \pm 0.19c$ to $1.25c \pm 0.13c$ (Figs. 5g–5i). Features B-NM and B-SM constitute a bright ridge running across the jet, and these features have the largest speeds of $1.25c \pm 0.13c$ and $0.92c \pm 0.09c$, respectively. Feature B-SW is an elongated feature extending toward knot C, and it has a somewhat lower speed of $0.75c \pm 0.12c$. Feature B-NE is adjacent to knot A and has a speed more similar to it, of $0.53c \pm 0.11c$. The last feature, B-SE, is quite different from the rest in that it shows motion toward the nucleus ($-0.21c \pm 0.19c$), though given the uncertainty it is also consistent with being stationary. If our uncertainties have been properly estimated, the dispersion in speeds would appear to be quite significant. A χ^2 test gives a probability of 1.1×10^{-9} for single speed in knot B.

Several regions of knots A and B (A-M, A-W, B-NM, B-MS, and B-SW) all have their velocity vectors significantly misaligned with the jet axis (Fig. 7c). This is consistent with the trend noted above: the inner jet from the nucleus to knot A appears straight and well collimated, and tends to show velocity vectors pointing directly away from the nucleus. Regions farther out (knots A, B, and C), where the jet curves and bends, show velocity vectors which are significantly misaligned with respect to the jet axis. Again, this suggests a connection between jet morphology and velocity field.

There is also evidence for variations in the structure of the $0\overset{''}{.}5$ long jet which extends westward from the unresolved core. While this jet has no distinct features or condensations, it does appear to lengthen with time. If we apply the cross-correlation algorithm to this region, we obtain axial and transverse speeds of $0.64c \pm 0.03c$ and $0.024c \pm 0.006c$, respectively. These results for the nuclear jet require confirmation by higher resolution observations, such as with *HST* or VLBA.

The jet region about $1''$ from the nucleus also shows significant structural changes between 1985 and 1993. The earlier epochs show only two compact knots in this region, about $1\overset{''}{.}1$ and $1\overset{''}{.}4$ from the nucleus, but by 1993 a third compact knot has appeared $0\overset{''}{.}86$ from the nucleus (Fig. 1c). Derivation of velocities for this region are more difficult, since the structural changes are large and the features are poorly resolved. A conservative interpretation of the structural variation gives a speed of $\sim 2.1c$ for the $1\overset{''}{.}1$ compact knot, but other interpretations are possible. Again, higher resolution observations are needed to study structural changes and velocities in this region. A forthcoming paper, containing additional epochs, will give more complete discussion of structural changes and brightness variations throughout the jet (Zhou, Biretta, & Owen 1995).

4. DISCUSSION

The results presented here give the first definitive evidence for motion in a kiloparsec-scale jet. Interpreted in the simplest way, these motions would appear to be a direct confirmation of the proposition by Rees (1971) that jets transport energy from galactic nuclei to the large-scale radio lobes.

The most natural explanation of the observed motions in M87 is that they are driven by fluid flow in the jet with speeds approaching c, the velocity of light. The predominance of outward motion, motion nearly parallel to the jet axis, and average speeds near $0.5c$, all seem plausible in such a picture. Knots D and B both show evidence of large velocity dispersions about the average speeds, ranging to over $2c$ in the case of knot D. One explanation for this large dispersion is that much of the emission arises in a thin boundary near the jet's surface (e.g., OHC89; BSH91). The dispersion might result from a turbulent shear between the jet and the external medium. Thus the observed speeds represent some middle ground between the underlying relativistic bulk relativistic flow and stationary external material.

One point which merits discussion is the possibility that random brightness fluctuations might give false evidence for motion. Since the jet features generally move only a minute fraction of their size during these observations, it is conceivable that random brightness fluctuations might give a false appearance of motion. However, there are several arguments which suggest such "Christmas tree" effects (Dent 1972) are relatively unimportant. First, outward speeds predominate with typical speeds near $0.5c$, and maximum speeds exceeding $2c$; *inward* speeds are rare and the largest speeds are merely $\sim 0.2c$. If Christmas tree effects were important, we would expect to see inward motion as frequently as outward motion, and of similar magnitudes. Second, in regions with the largest axial speeds, the transverse motions appear to be relatively small. If we attributed the large axial speeds to random brightness variations, we might expect to see equally large transverse speeds. Third, it is common for adjacent features to have similar speeds, and this would not be expected if the motions were derived from random brightness fluctuations. Examples are regions D-M and D-W, all regions in knot A, and B-NM and B-SM. And finally, the features with the most significant motion detections (A-N, A-S, and B-NM) give evidence of constant velocity, which would not be expected if random brightness fluctuations were important. These arguments together suggest the observed motions in M87 cannot be caused solely by Christmas tree effects, and that they are instead related to physical motions in the jet.

It is still possible, at least in principle, that Christmas tree effects might play some role in causing the internal velocity dispersions seen in several knots. For example, one might imagine the knots moving near the average speed $\sim 0.5c$, and that random brightness fluctuations provide the observed differences from that speed. This may be possible in knot B, where differences from this mean velocity would range from $-0.7c$ to $+0.7c$. But it seems much less likely in knot D, where the dispersion about $0.5c$ would still be highly anisotropic and strongly favor motion away from the nucleus. Hereafter we will assume that Christmas tree effects are unimportant and that the observed motions are related to physical motions within the jet.

We now examine constraints on jet velocities derived from the observed motions and other effects. Since the velocities of patterns in the jet may be different from those of the jet fluid (e.g., Lind & Blandford 1985), we consider the pattern and fluid speeds, $\beta_{pattern}$ and β_{fluid}, separately. After deriving constraints on these velocities in M87, we will outline a possible model for the kinematics in M87 and discuss its implications for other radio sources.

4.1. Constraints on Pattern Speeds of Observed Features and Jet Orientation

The observed speeds in units of the velocity of light, β_{obs}, can be related to the pattern speed $\beta_{pattern}$ in the comoving frame and the angle θ between the line of sight and the velocity vector through the usual relationship for superluminal motion (Blandford & Königl 1979),

$$\beta_{obs} = \frac{\beta_{pattern} \sin \theta}{1 - \beta_{pattern} \cos \theta}. \qquad (2)$$

The two regions essential to the present discussion, D-M and A-E, have small transverse speeds relative to their axial speeds. Hence we set $\beta_{obs} = v_x/c$, and assume their velocity vectors are directed parallel to the jet axis.

For a given observed speed β_{obs} there exists a minimum possible $\beta_{pattern}$ and a maximum possible θ (e.g., Pearson & Zensus 1987). Table 4 summarizes these derived constraints for several jet regions. Knot A shows the most significant evidence for motion, $\beta_{obs} \sim v_x/c = 0.509 \pm 0.015$, where c is the velocity of light. This requires $\beta_{pattern} > 0.454 \pm 0.011$, a corresponding Lorentz factor $\gamma_{pattern} > 1.122 \pm 0.007$, and $\theta < 126°.0 \pm 1°.4$. Larger observed speeds give stronger constraints. The largest speed in region D-M, $v_x = 2.51c \pm 0.28c$, implies $\gamma_{pattern} > 2.7 \pm 0.26$ and $\theta < 43° \pm 4°$.

The appearance of a bright, linear feature across the jet in knot A can provide an additional constraint on the jet's geometry and speed. One reasonable assumption is that this

TABLE 4

CONSTRAINTS DERIVED FROM OBSERVED AXIAL VELOCITIES v_x

Region	$\beta_{obs} = v_x/c$	$\beta_{pattern}$	$\gamma_{pattern}$	θ
Knot A	0.509 ± 0.015	$>0.454 \pm 0.011$	$>1.122 \pm 0.007$	$<126°.0 \pm 1°.4$
A-E	0.479 ± 0.019	$>0.432 \pm 0.014$	$>1.109 \pm 0.008$	$<128.8 \pm 1.8$
Knot B	0.62 ± 0.05	$>0.53 \pm 0.03$	$>1.18 \pm 0.03$	$<116 \pm 4$
B-NM	1.25 ± 0.13	$>0.78 \pm 0.03$	$>1.60 \pm 0.10$	$<77 \pm 6$
B-SM	0.92 ± 0.09	$>0.68 \pm 0.04$	$>1.36 \pm 0.06$	$<95 \pm 6$
Knot D	0.41 ± 0.10	$>0.38 \pm 0.08$	$>1.08 \pm 0.04$	$<135 \pm 10$
D-M	2.51 ± 0.28	$>0.929 \pm 0.014$	$>2.70 \pm 0.26$	$<43 \pm 4$
D-W	2.10 ± 0.22	$>0.903 \pm 0.018$	$>2.33 \pm 0.20$	$<51 \pm 5$

linear feature is, in reality, a two-dimensional structure seen in projection. This structure might be either a filament wrapped around the jet, so as to form a ring or helix with small pitch angle (e.g., OHC89), or it might be a disklike structure (e.g., Mach disk; BOH83; Eichler & Smith 1983). Such structures define a plane in three dimensions, which projects into the narrow linear feature we observe across the jet. A constraint results, since this moving structure must maintain an edge-on appearance in the presence of relativistic aberration. That is, this assumed geometry requires the observed photons leaving the farthest portion of the planar structure to pass through the nearest portion of the structure, so as to maintain the narrow appearance of this feature. For the simplest case where the plane is normal to the jet axis, a coincidence is required between θ and $\beta_{pattern}$ such that $\beta_{pattern} = \cos(\theta)$; (BOH83). A more generalized geometry might allow the plane containing the edge to be at some angle $90° + \epsilon$ to the jet axis (Reid et al. 1989; BOC89) and the resulting constraint is

$$\cot \theta = \frac{\tan \epsilon + \beta_{pattern} \sec \epsilon}{\sqrt{1 - \beta_{pattern}^2}}. \qquad (3)$$

The observed angle between the edge and the jet axis measured on the plane of the sky is $\sim 72°$, suggesting $|\epsilon|$ could be at least $18°$. We will adopt $|\epsilon| \leq 30°$ as a maximum value. The combinations of θ and $\beta_{pattern}$ allowed by this constraint are illustrated in Figure 8. The constraint from the observed motion of this feature (region A-E) is also plotted, and we show the region allowed by 1 σ uncertainties. The two constraints for knot A together require the angle between the jet axis and the line of sight, $38° \lesssim \theta \lesssim 93°$, and a pattern speed for the edge of $0.42 \lesssim \beta_{pattern} \lesssim 0.50$.

(We note that knot C also shows a linear feature transversing the jet, but it appears curved and less sharp than the feature in knot A. It also has lower fractional polarization than knot A. These qualities are consistent with a less "edge-on" orientation, as would be expected if its θ were similar to knot A's while suffering less aberration since $v_x \sim 0.1c$ for knot C.)

If the jet is assumed straight in three dimensions between knots D and A, which is how it appears on the sky plane, we
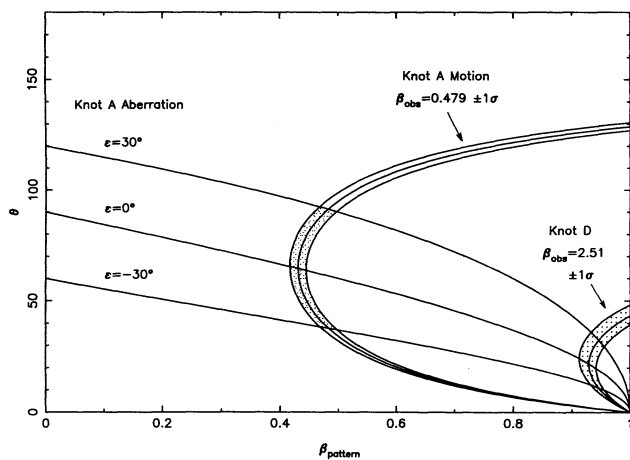

FIG. 8.—Constraints on angle between the jet axis and line-of-sight θ and pattern speed of jet features, $\beta_{pattern}$. These are derived from (a) observed motion of knot A edge at $\beta_{obs} = 0.479$, (b) appearance of narrow linear feature in knot A coupled with relativistic aberration ($|\epsilon| < 30°$), and (c) observed motion of feature D-M at $\beta_{obs} = 2.5$. The constraints for knots A and D, taken together, imply $\theta = 42°.5 \pm 4°.5$.

may further assume the same value of θ for both these regions. We may thus combine this constraint on θ with that derived from the proper motion of region D-M, $\theta < 43° \pm 4°$ (Table 4). Together these constraints require a jet orientation $\theta = 42°.5 \pm 4°.5$ to the line of sight.

Ford et al. (1994) have studied a disk of gas surrounding the nucleus of M87. By assuming a circular disk and deprojecting its elliptical appearance, they deduce an angle between the disk axis and line of sight of $42° \pm 5°$. This is in good agreement with the orientation we find, and suggests the jet is almost exactly normal to the circumnuclear gas disk.

4.2. Constraints on the Speed of the Jet Fluid

So far we have considered only the *pattern* speeds of features in the jet. The more interesting parameter is the speed of the jet *fluid* itself. Here the arguments are unfortunately less direct. Nonrelativistic numerical simulations of jets (e.g., Norman, Winkler, & Smarr 1984) have found that the fluid speed tended to exceed that of the visible patterns. From the derived pattern speeds $\beta_{pattern} \gtrsim 0.5$ in much of the jet, this would appear to imply at least $\beta_{fluid} \gtrsim 0.5$, and perhaps $\beta_{fluid} \sim 1$ for regions where superluminal motion is seen. Other indirect evidence can be taken from statistical studies of superluminal quasars, where Cohen (1990) finds similar mean values for the Lorentz factors of the fluid and pattern.

We also note that "scissor effects," which are sometimes cited as a possible cause of $\beta_{pattern} > \beta_{fluid}$ (e.g., Hardee & Norman 1989; Fraix-Burnet 1990), must be relatively unimportant in the M87. A scissor effect might be created, for example, at the intersection of a pair of shock waves. While the individual waves might move slowly, their intersection defines a pattern which could attain any speed. However, the predominance of outward motion in the jet argues against such a scheme. Furthermore, the fastest jet features move nearly parallel to the jet axis. For such a model to be tenable in M87, there would need to be an additional contrivance which restricted these shock intersections to move only parallel to the jet axis. It would seem far more natural to have the observed motions tied to the jet flow, with $\beta_{pattern} \lesssim \beta_{fluid}$.

Another line of evidence on the fluid speed, β_{fluid}, comes from the absence of a visible counterjet. Recently, optical emission has been detected from a small region directly opposite the jet in the east radio lobe (Sparks et al. 1992; Stiavelli et al. 1992a), and this has been interpreted as the terminus of an unseen counterjet. The lifetime against synchrotron emission is of order 10^3 yr; so, unlike the radio emission in the east lobe, this optical emission cannot be attributed to events in the distant past. Some supply of optically emitting synchrotron electrons would be required at the present epoch. The radio-to-optical spectral index of this region is identical to that seen in the jet at a similar core distance (25"), which further suggests the optical feature in the east lobe might be related to a counterjet.

If we assume the putative counterjet is intrinsically similar to the jet and is hidden by relativistic beaming effects, the observed limit on the jet/counterjet brightness ratio R provides a constraint on β_{fluid} and θ,

$$R = \left(\frac{1 + \beta_{fluid} \cos \theta}{1 - \beta_{fluid} \cos \theta}\right)^{2.5}, \qquad (4)$$

where the exponent 2.5 assumes a radio spectral index $\alpha = -0.5$ where $S_\nu \propto \nu^\alpha$ (BSH91). Taking the ratio of mean jet

brightness to the mean brightness in a similar counterjet region in a radio image, and allowing for subtraction of a background level, gives the limit $R > 150$ (BOC89). (Optical observations give a stronger limit $R > 450$ [Stiavelli, Moller, & Zeilinger 1992b], but the exponent in eq. [4] increases to 3.2, resulting in a weaker constraint.) Using the constraint $R > 150$ derived from the radio data, we obtain $\beta_{\rm fluid} > 0.76$ ($\gamma_{\rm fluid} > 1.5$) and $\theta \lesssim 40°$. This orientation is consistent with that derived above. The main uncertainty with this calculation, of course, is the assumption that the unseen counterjet has an intrinsic brightness similar to the visible jet. It is entirely possible that the counterjet is intrinsically faint, in which case the constraint is weakened.

4.3. A Possible Model for the Kinematics of the M87 Jet

While many details of the kinematics remain obscured, it is interesting to speculate regarding a kinematic model for the jet. We now consider the following hypothetical model: the inner jet (nucleus to knot A) contains a high Mach number flow with a Lorentz factor $\gtrsim 3$ and oriented about 42° from the line of sight. A strong shock at knot A (~ 1 kpc from the nucleus) reduces the flow speed to $\gamma_{\rm fluid} < 2$. A second shock in knot C further reduces the jet speed such that beaming becomes unimportant, and at larger distances the jet forms a subsonic, buoyant plume.

Much of the evidence for such a picture arises from the morphology and polarization properties of the jet. The inner jet is quite straight (< 1.2 kpc), but at knot A the morphology suddenly changes and the jet bends and kinks. Knot C appears to induce further "instability" and sharp bends in the outer jet (> 1.6 kpc). This increasing instability after each of knots A and C suggests a reduction in the jet's Mach number. Moreover, both knots A and C contain bright linear features transverse to the jet axis which are suggestive of Mach disks or shocks. Polarization data indicate the magnetic fields are parallel to these linear features, which is further consistent with the presence of shocks. Hence the morphology would seem consistent with a high Mach number inner jet, followed by shocks in knots A and C which substantially reduce the flow speed.

A natural explanation for superluminal motion in knot D would be the presence of an underlying flow with $\gamma \gtrsim 3$. Hence, the high Mach number inner jet would, in this picture, be a relativistic flow. Knot A would thus be a relativistic shock, for which the downstream fluid speed is $c/3$ relative to the shock (Blandford & Rees 1974). Taking $\theta \sim 42°$, this implies an apparent speed of $0.9c$ for the downstream material, which is at least roughly consistent with the larger observed motions in knot B.

One concern about such a model is the slow proper motions seen in the nucleus by VLBI techniques. Component N2 appears to move outward at only $\sim 0.3c$ (Reid et al. 1989), and components even closer to the core appear nearly stationary (Junor & Biretta 1995). This could be attributed to $\beta_{\rm pattern} \ll \beta_{\rm fluid}$, for example, if the VLBI knots in M87 were "fixed" features excited by, or tied to, the external medium. This makes M87 rather different from quasar nuclei where $\beta_{\rm pattern} \sim \beta_{\rm fluid}$ seems common (Cohen 1990). One explanation for the difference might be the $\sim 42°$ angle from the line of sight in M87. For $\theta \sim 42°$ and $\gamma_{\rm fluid} = 3$, Doppler beaming causes almost no brightness enhancement, and for $\gamma_{\rm fluid} > 3.5$, features actually appear dimmer than in the comoving frame. The large angle places Earth outside the Doppler beaming cone for any fea-

tures in the M87 nucleus with $\gamma_{\rm pattern} \approx \gamma_{\rm fluid} \gtrsim 3$. Superluminal quasars, on the other hand, are thought to be oriented very near the line of sight and have the brightness of their superluminal features strongly enhanced by beaming. We also note that cases of "slow" or stationary features in superluminal jets are not unknown, for example in 4C 39.25 (Shaffer & Marscher 1987). Alternatively, there could be an acceleration (Daly & Marscher 1988) between the parsec and kiloparsec scales in M87.

Another concern regards the disposition of the inner jet's bulk kinetic energy after knot A. If the jet is suddenly decelerated at knot A, where is this energy going? It does not seem to go into radiation, since the luminosity of knot A is not that much greater than that of the other knots. Furthermore, the jet remains collimated, so it probably does not go into internal pressure. However, it is unclear how much kinetic energy is being carried by the inner jet; it is possible that the jet is very light (i.e., low mass density) and therefore carries relatively little bulk kinetic energy. A related concern is the high luminosity of the lobes, which is presumably supplied by the jet. However, this luminosity is dominated by low-frequency radio emission, and these electrons have extremely long lives. It may be adequate to merely supply energetic electrons, rather than bulk kinetic energy, to the lobes. If we ignore adiabatic expansion and assume that luminous plasma flowing through knot B at $\beta \sim 0.7$ merely inflates the lobes, then the lobe luminosity could be supplied in 10^5 yr, which is less than electron lifetimes at radio frequencies.

A model of this type may have several additional benefits. It is well known that the optical emission from the outer knots presents a problem—the particle lifetimes are much shorter than the light-travel time from the nucleus. In the model we have outlined, time dilation effects associated with relativistic flow along the inner jet would allow energetic electrons to travel farther from the nucleus, thereby reducing the particle lifetime problem (Biretta & Meisenheimer 1993). The knot spectra are similar until knot A, at which point they steepen systematically with increasing distance; this could be attributed to a sudden large reduction in the jet velocity at knot A.

In terms of other F-R I radio sources, a relativistic "inner jet" might account for the one-sided jet "bases" seen in many of these sources (Bridle 1986). These one-sided bases are typically straight, well collimated, and 2–20 kpc in length (e.g., Bridle 1984; Eilek et al. 1984; Leahy, Jagers, & Pooley 1986; O'Dea & Owen 1986), and thus resemble the inner jet of M87. Only on larger scales does the structure become two-sided and poorly collimated, and suggest nonrelativistic flow (e.g., Scheuer 1987). Similarly, a relativistic inner jet would also explain the one-sided jets in the nuclei of F-R I sources (Giovannini et al. 1994).

A relativistic inner jet would also be consistent with $\gamma \gtrsim 5$ on the parsec scale, as required by unified models which propose that radio galaxies are the parent population of BL Lac objects (Browne 1983; Urry, Padovani, & Stickel 1991, and references therein). Our observations suggest $\gamma_{\rm fluid} \gtrsim 3$, and would be consistent with larger values. We note that for the derived orientation angle $\theta \sim 42°$, any regions with $\gamma_{\rm fluid} \gg 3$ would be strongly dimmed by Doppler beaming away from the observer, and hence the absence of large superluminal motions does not argue against larger γ.

A final point regards transverse motions and their implications for statistics of superluminal radio sources. Feature D-W appears to have superluminal motion directed about 6° to the

jet axis, or about 4° if one deprojects assuming an angle $\theta \sim 37°$. Importantly, this motion appears to be along an elongated structure at that point in the jet, which can be interpreted as a filament wrapped around the jet (OHC89). This suggests a situation in which superluminal features need not move directly away from the nucleus, but instead might move along filamentary structures within a jet or wrapped around a jet, and hence have a range of velocity directions about the jet axis. For M87 ($\beta_{apparent} \sim 2$) a few degrees difference between the velocity vector and jet axis would have only minor consequences, but in superluminal quasars the effect could be profound. For example, 3C 345 has motion at $\beta_{apparent} \sim 10$ which implies $\theta < 11°$ (Biretta, Moore, & Cohen 1986). If filamentary structures cause a $\pm 4°$ range in the velocity direction, the solid angle available for detection of superluminal motion at $10c$ is doubled. Moreover, such filamentary structures might be wrapped tightly around a jet (i.e., with large pitch angle), so the angle between the velocity vector and jet axis could also become quite large. Such effects would have significant impact on the statistical properties of superluminal sources (e.g., Cohen 1990).

5. SUMMARY

Our results may be summarized as follows:

1. We detect outward motion throughout the M87 jet. Most knots show average speeds around $0.5c$, though knot C, which is located near the terminus of the jet, is much slower with $v = 0.11c \pm 0.04c$. These motions would appear to directly confirm the accepted view of extragalactic sources in which energy flows from the nucleus, along jets, and into the extended radio structure.

2. Measurements on small features within knots B and D reveal large internal velocity dispersions for these knots. Two regions in knot D display superluminal motion exceeding $2c$, while apparent speeds in knot B range from $-0.2c$ to $+1.2c$.

3. Motions transverse to the jet axis are also seen. Transverse motions become especially significant near the end of the jet, in the same regions where the jet appears to bend and oscillate from side-to-side.

4. The observed motion and presence of a narrow linear feature in knot A, together with the superluminal motion in knot D, constrain the jet to lie at $\theta \approx 43°$ from the line of sight. This places the jet nearly perpendicular to the disk of circumnuclear gas.

5. Velocities measured in the kiloparsec-scale jet are much larger than seen at the parsec-scale with VLBI. The jet must either accelerate between these scales, or the features seen with VLBI move much slower than the bulk flow speed.

6. We outline a kinematic model for the jet wherein the first kiloparsec consists of a relativistic flow ($\gamma \gtrsim 3$) followed by sudden deceleration in knots A and C. Such a picture would appear to account for some properties of other F-R I radio sources.

Future VLA monitoring of the M87 jet will allow proper motion measurements for faint regions in the jet and perhaps also in the extended radio lobes. It may also be possible to detect accelerations in some of the bright regions already studied. Optical monitoring with *HST*, to the extent that the optical emission appears more concentrated near the jet axis (Biretta 1994; Sparks, Biretta, & Macchetto 1995), will allow measurement of the velocity field in a physical volume near the jet axis, thus providing clues as to the jet's radial velocity structure. The high resolution of *HST* ($\sim 0''.03$) will also allow monitoring of the jet's first few arcseconds, where rapid structural changes are seen, but where the details are poorly resolved by the present VLA data.

REFERENCES

Begelman, M. C., Blandford, R. D., & Rees, M. J. 1984, Rev. Mod. Phys., 56, 255
Bevington, P. R. 1969, Data Reduction and Error Analysis for the Physical Sciences (New York: McGraw-Hill), 85
Biretta, J. A. 1994, in Astrophysical Jets, ed. D. Burgarella, M. Livio, & C. P. O'Dea (Cambridge: Cambridge Univ. Press), 263
Biretta, J. A., & Meisenheimer, K. 1993, in Jets in Extragalactic Radio Sources, eds. H.-J. Röser & K. Meisenheimer (Berlin: Springer-Verlag), 159
Biretta, J. A., Moore, R. L., & Cohen, M. H. 1986, ApJ, 308, 93
Biretta, J. A., & Owen, F. N. 1990, in Parsec-scale Jets, ed. J. A. Zensus & T. J. Pearson (Cambridge: Cambridge Univ. Press), 125
Biretta, J. A., Owen, F. N., & Cornwell, T. J. 1989, ApJ, 342, 128 (BOC89)
Biretta, J. A., Owen, F. N., & Hardee, P. E. 1983, ApJ, 274, L27 (BOH83)
Biretta, J. A., Stern, C. P., & Harris, D. E. 1991, AJ, 101, 1632 (BSH91)
Blandford, R. D., & Königl, A. 1979, ApJ, 232, 34
Blandford, R. D., & Rees, M. J. 1974, MNRAS, 169, 395
Bridle, A. H. 1984, AJ, 89, 979
————. 1986, Canadian J. Phys., 64, 353
Bridle, A. H., & Perley, R. A. 1984, ARA&A, 22, 319
Briggs, D. S., Usowicz, J., & Cornwell, T. J. 1991, private communication
Browne, I. W. A. 1983, MNRAS, 204, p23
Cohen, M. H. 1990, in Parsec-Scale Jets, ed. J. A. Zensus & T. J. Pearson (Cambridge: Cambridge Univ. Press), 317
Cornwell, T. J. 1983, A&A, 121, 281
Daly, R. A., & Marscher, A. P. 1988, ApJ, 334, 539
Dent, W. A. 1972, ApJ, 175, L55
Eichler, D., & Smith, M. 1983, Nature, 303, 779
Eilek, J. A., Burns, J. O., O'Dea, C. P., & Owen, F. N. 1984, ApJ, 278, 37
Fanaroff, B. L., & Riley, J. M. 1974, MNRAS, 167, 31P
Ford, H. C., et al. 1994, ApJ, 435, L27
Fraix-Burnet, D. 1990, A&A, 227, 1

Giovannini, G., et al. 1994, in Compact Extragalactic Radio Sources, ed. J. A. Zensus & K. I. Kellermann (Socorro: NRAO), 61
Gull, S. F., & Skilling, J. 1984, in Indirect Imaging, ed. J. A. Roberts (Cambridge: Cambridge Univ. Press), 267
Hardee, P. E., & Norman, M. L. 1989, ApJ, 342, 680
Junor, W., & Biretta, J. A. 1995, AJ, 109, 500
Leahy, J. P., Jagers, W. J., & Pooley, G. G. 1986, A&A, 156, 234
Lind, K. R., & Blandford, R. D. 1985, ApJ, 295, 358
Ma, C., Shaffer, D. B., de Vegt, C., Johnston, K. J., & Russell, J. L. 1990, AJ, 99, 1284
Mould, J., Aaronson, M., & Huchra, J. 1980, ApJ, 238, 458
Muxlow, T. W. B., & Wilkinson, P. N. 1991, MNRAS, 251, 54
Napier, P. 1991, private communication
Narayan, R., & Nityananda, R. 1986, ARA&A, 24, 127
Norman, M. L., Winkler, K.-H. A., & Smarr, L. 1984, in Physics of Energy Transport in Extragalactic Radio Sources, ed. A. H. Bridle & J. A. Eilek (Green Bank: NRAO), 150
O'Dea, C. P. 1985, ApJ, 295, 80
O'Dea, C. P., & Owen, F. N. 1986, ApJ, 301, 841
Owen, F. N., Hardee, P. E., & Cornwell, T. J. 1989, ApJ, 340, 698 (OHC89)
Pearson, T. J., & Zensus, J. A. 1987, in Superluminal Radio Sources, ed. J. A. Zensus & T. J. Pearson (Cambridge: Cambridge Univ. Press), 1
Perley, R. A. 1984, in VLBI and Compact Radio Sources, ed. R. Fanti, K. Kellermann, & G. Setti (Dordrecht: Reidel), 153
Porcas, R. W. 1986, in Superluminal Radio Sources, ed. J. A. Zensus & T. J. Pearson (Cambridge: Cambridge Univ. Press), 12
Rees, M. J. 1971, Nature, 229, 312
Reid, M. J., Biretta, J. A., Junor, W., Spencer, R., & Muxlow, T. 1989, ApJ, 336, 125
Scheuer, P. A. G. 1987, in Astrophysical Jets and Their Engines, ed. W. Kundt (Dordrecht: Reidel), 129

Shaffer, D. B., & Marscher, A. P. 1987, in Superluminal Radio Sources, ed. J. A. Zensus & T. J. Pearson (Cambridge: Cambridge Univ. Press), 67
Sovers, O. J., et al. 1988, AJ, 95, 1647
Sparks, W. B., Biretta, J. A., & Macchetto, F. 1995, in preparation
Sparks, W. B., Fraix-Burnet, D., Macchetto, F., & Owen, F. N. 1992, Nature, 355, 804
Spencer, R. E., & Junor, W. 1986, Nature, 321, 753
Stiavelli, M., Biretta, J., Möller, P., & Zeilinger, W. W. 1992a, Nature, 355, 802
Stiavelli, M., Möller, P., & Zeilinger, W. W. 1992b, Nature, 354, 132

Thompson, A. R., Moran, J. M., & Swenson, G. W. 1986, Interferometry and Synthesis in Radio Astronomy (New York: Wiley & Sons), 411
Tonry, J. L. 1991, ApJ, 373, L1
Urry, C. M., Padovani, P., & Stickel, M. 1991, ApJ, 382, 501
van Maanen, A. 1916, ApJ, 44, 210
Walker, R. C. 1991, private communication
Walker, R. C., Walker, M. A., & Benson, J. M. 1988, ApJ, 335, 668
Zhou, F., Biretta, J. A., & Owen, F. N. 1995, in preparation

PLATE 19

Fig. 1.—(a) Final MEM images of M87 jet for epochs 1985 February 26 and 1993 January 11. Intensities have been adjusted so that knot A has similar brightness in both images. Knots are labeled with their usual letter designations. Up is toward P.A. 20°5. (b) Same as (a), but showing lower intensities. (c) Enlargement of inner jet including the core and knots D and E. Arrows indicate features which appear to change or move between 1985 and 1993; the arrows can be used as fiducial points for judging motions (see [a]).

Fig. 1a

Biretta, Zhou, & Owen (see 447, 584)

PLATE 20

FIG. 1b

Core

1985 Feb. 26

1993 Jan. 11

D E F I A B C

N

E

1"

Fig. 1c

PLATE 22
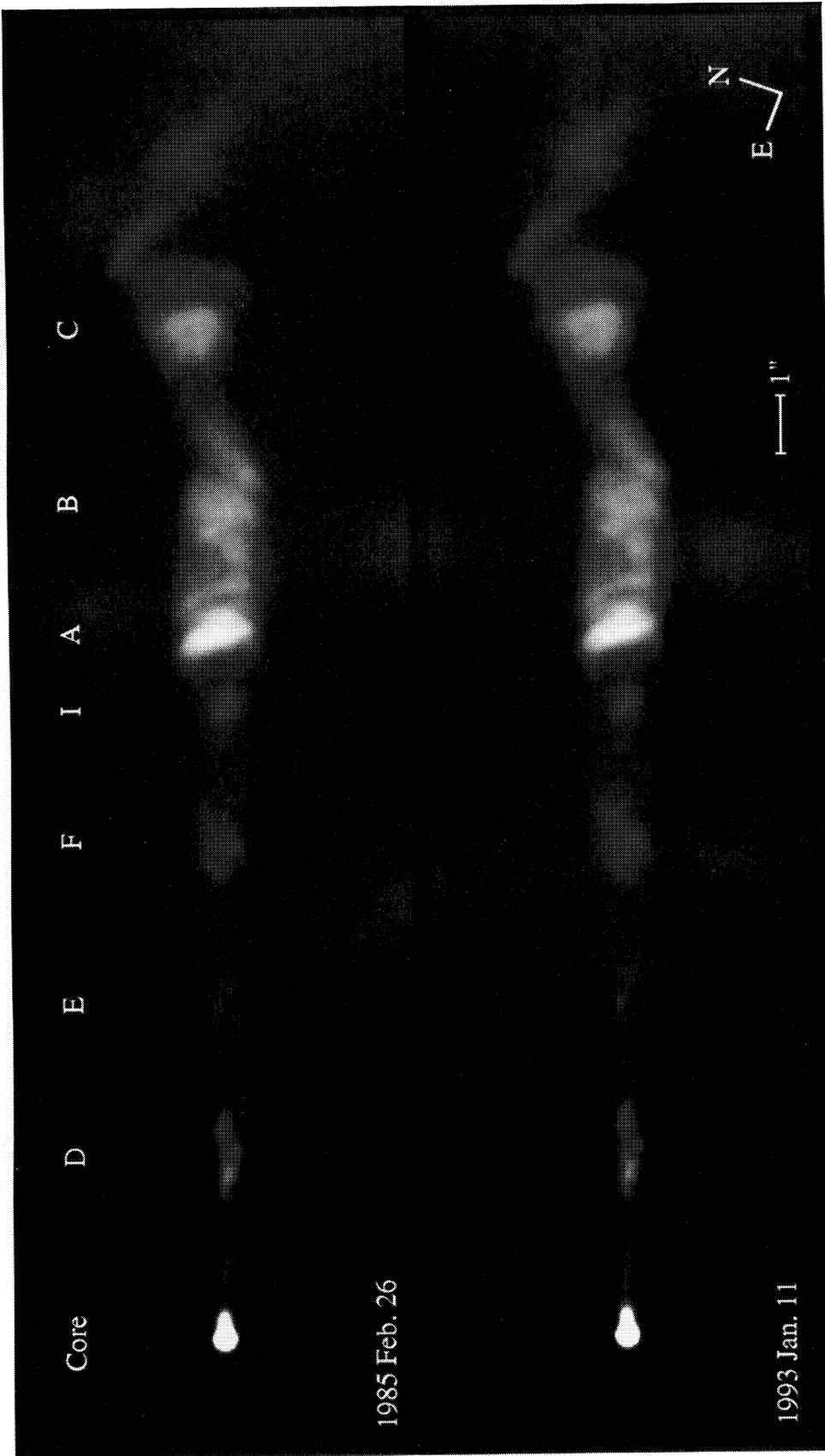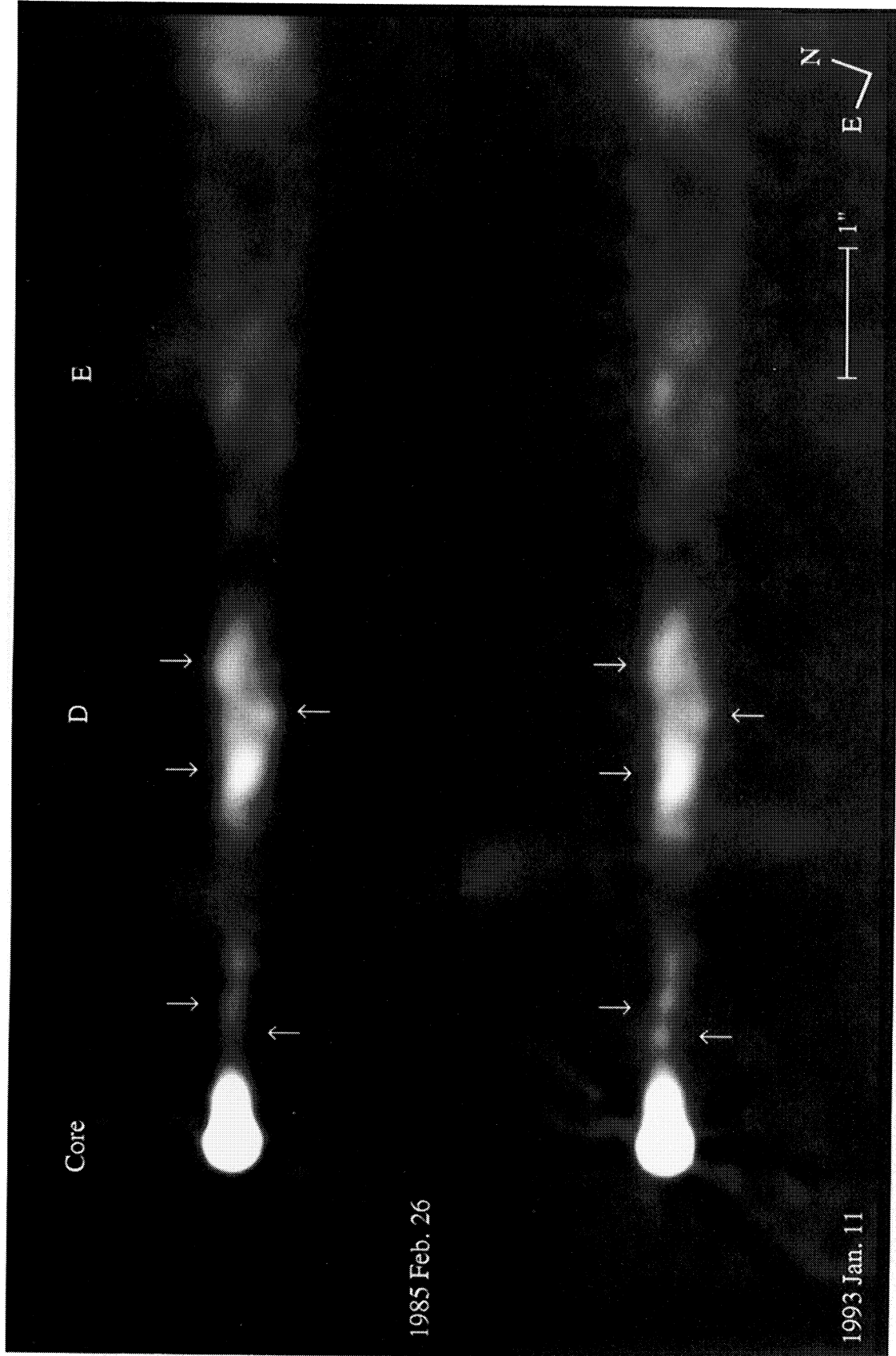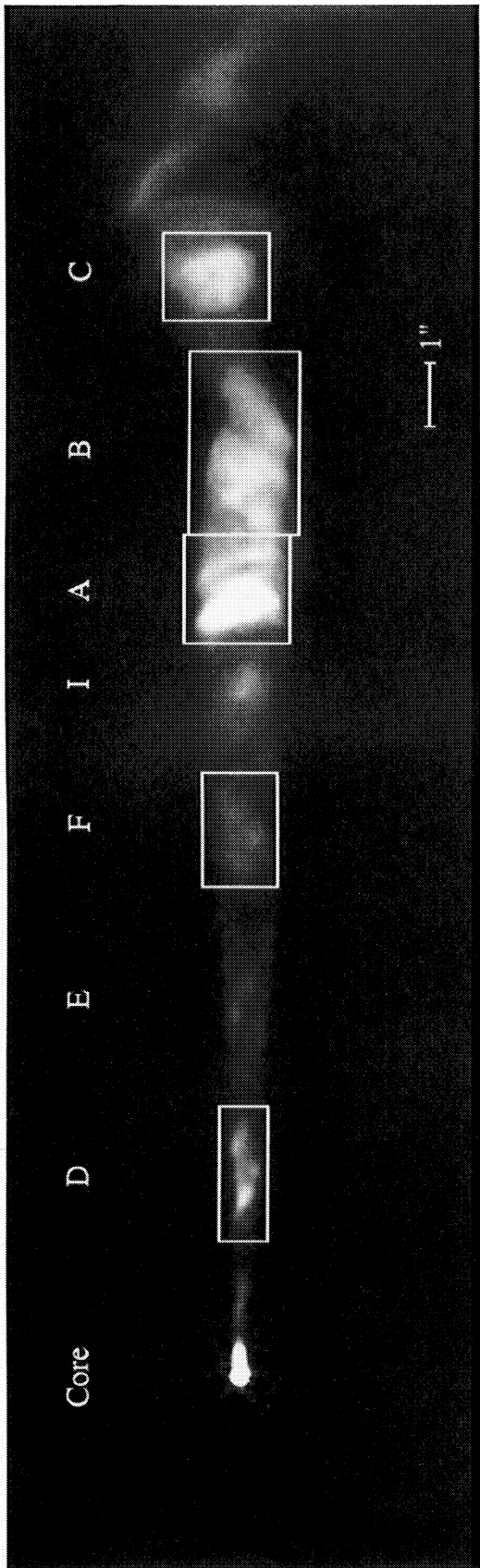
Fig. 2.—The regions used for measuring the velocities of knots D, F, A, B, and C are shown. This image was made with the MEM technique by combining all 1985 and 1989 (u, v) data.
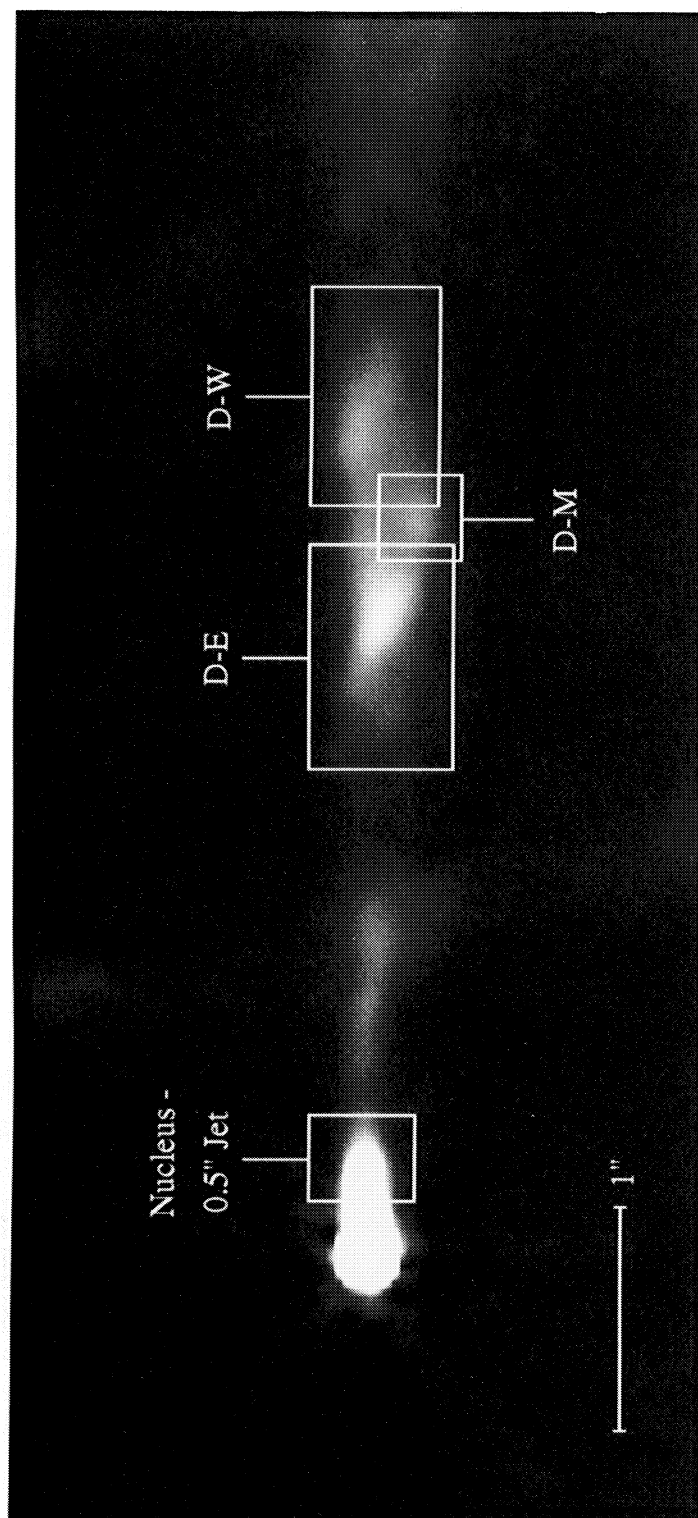
Biretta, Zhou, & Owen (see 447, 584)

PLATE 23

FIG. 3a

FIG. 3.—(a) The regions used for measuring motion of nuclear jet and regions within knot D. For epoch 1993 the box for D-M was enlarged 0″07 on the side away from the nucleus, to prevent this feature from leaving the cross-correlation box (same image as used in Fig. 2). (b) The regions used for measuring motion of features within knot A (same image as used in Fig. 2). (c) The regions used for measuring motions of features within knots A and B (same image as used in Fig. 2).

BIRETTA, ZHOU, & OWEN (see 447, 584)

PLATE 24
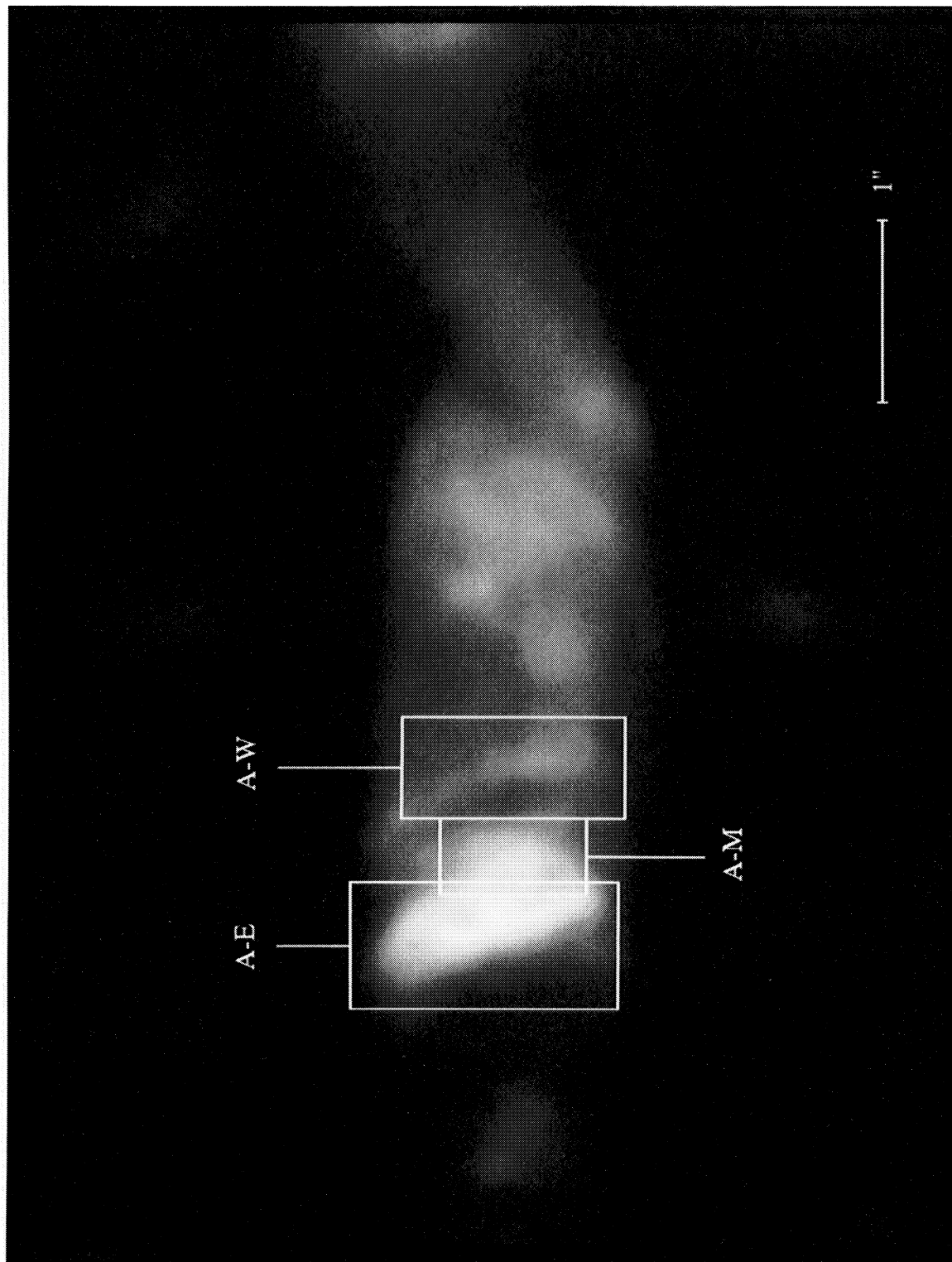
Fig. 3b

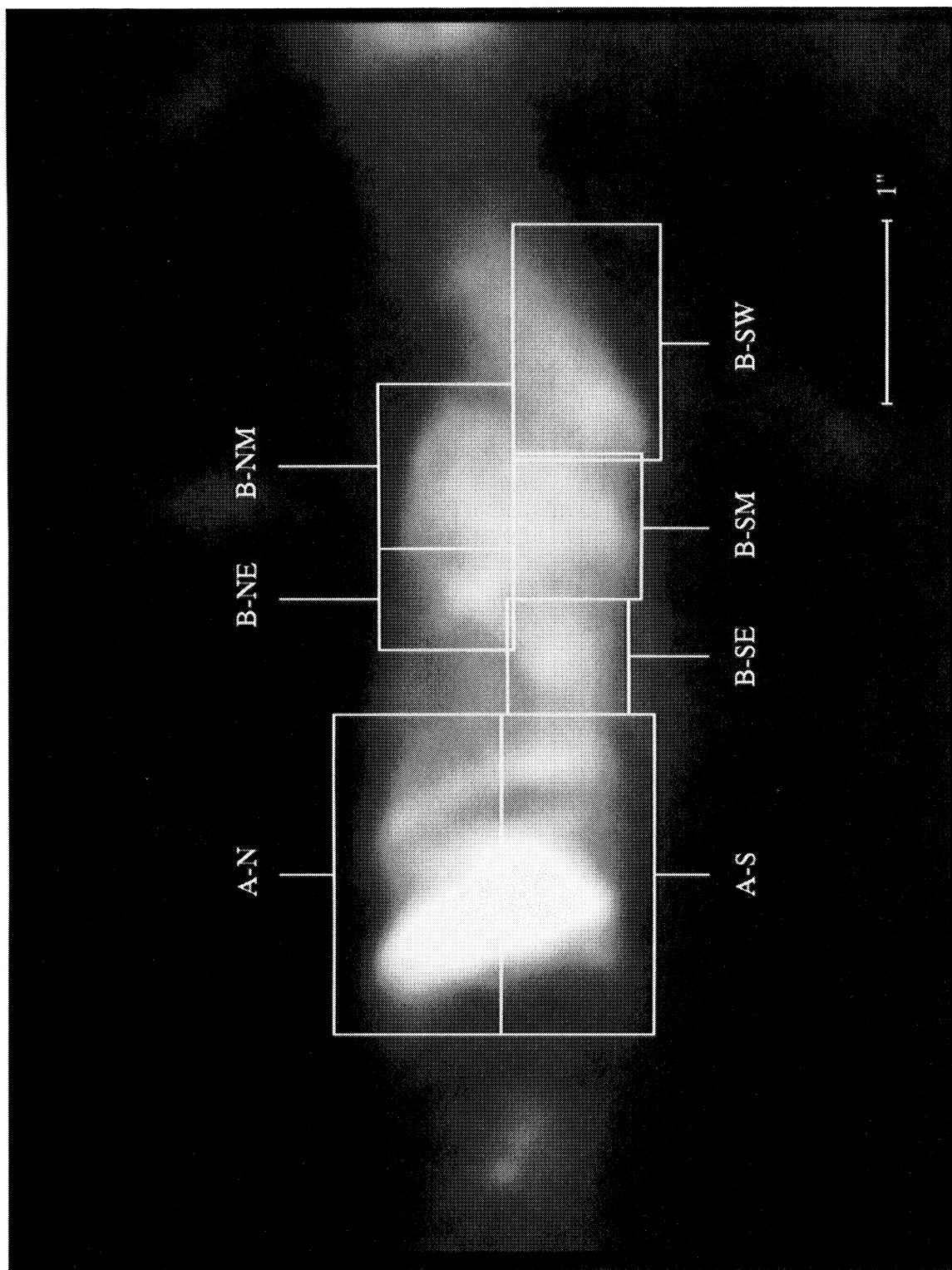Biretta, Zhou, & Owen (see 447, 584)

PLATE 25

FIG. 3c

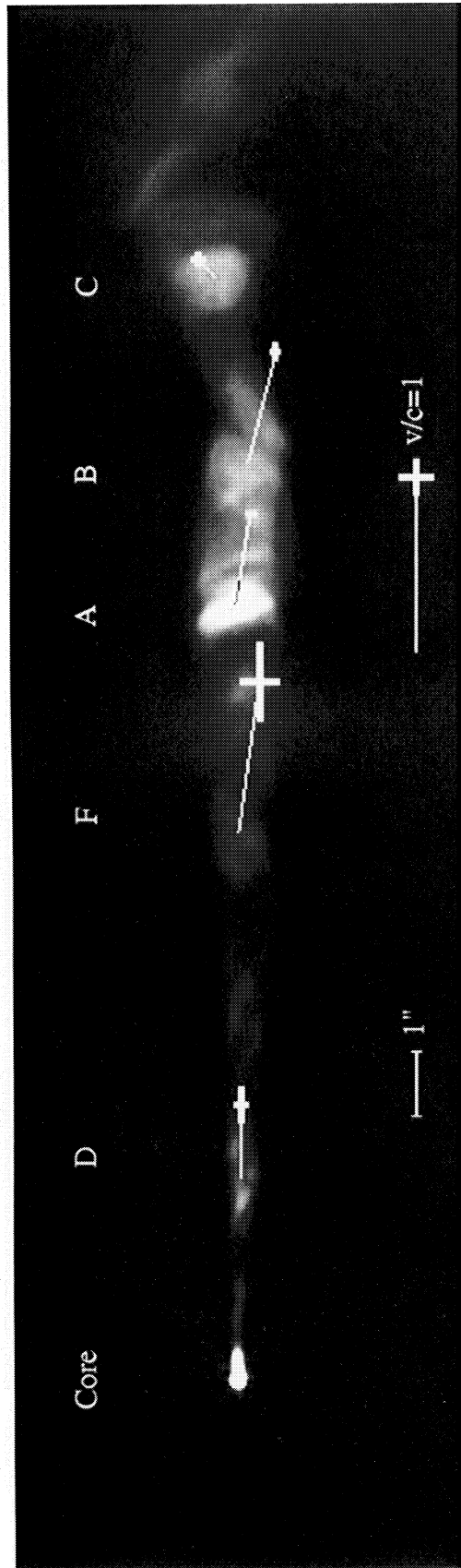BIRETTA, ZHOU, & OWEN (see 447, 584)

PLATE 26

FIG. 6.—Observed velocity vectors for entire knots D, F, A, B, and C superposed on image of the jet (image from Fig. 2). Motion direction is toward the heavy cross at the end of each vector, which indicates the 1 σ uncertainty on each component of the motion.
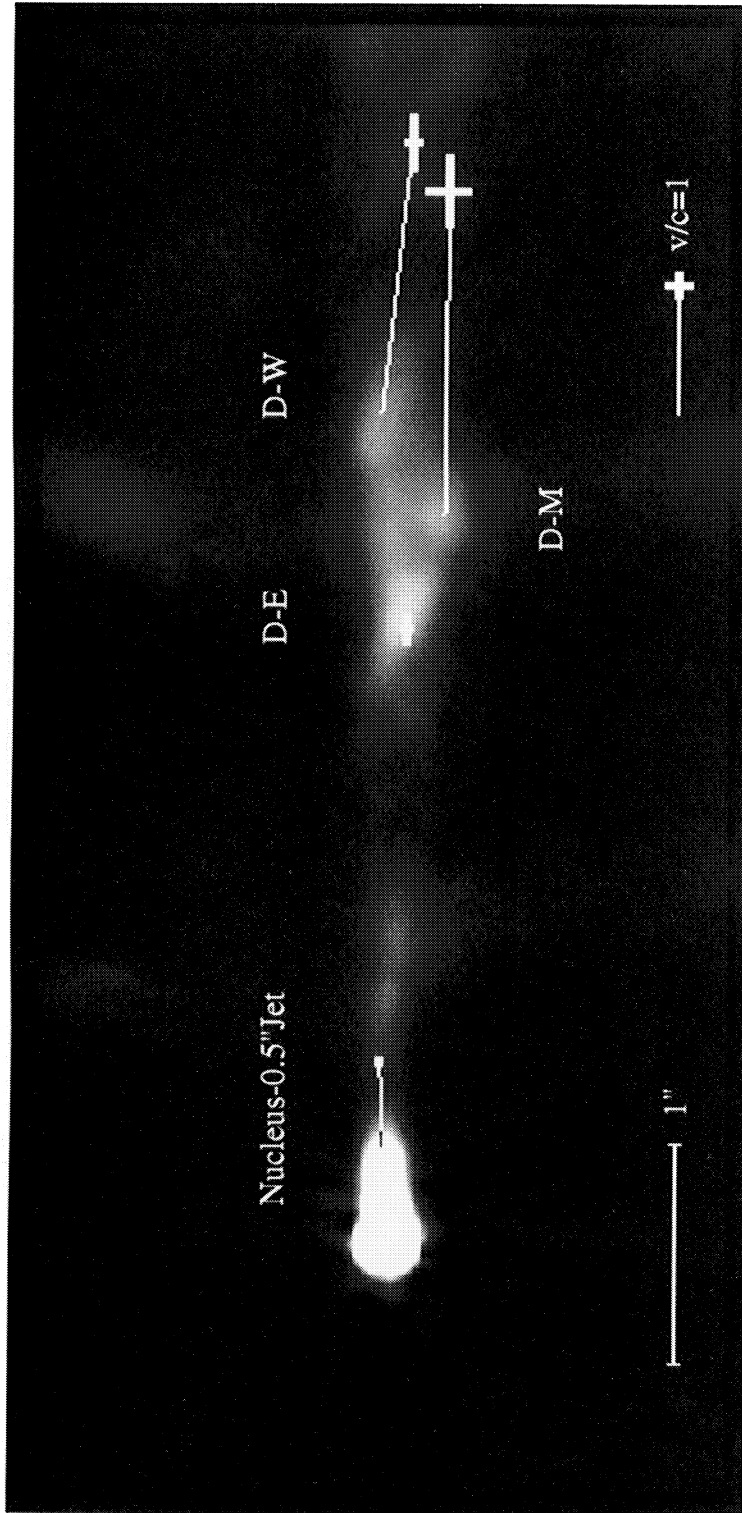
BIRETTA, ZHOU, & OWEN (see 447, 588)

Fig. 7a

FIG. 7.—Observed velocity vectors for features within knots superposed on an image of the jet. Motion direction is toward the heavy cross at the end of each vector, which indicates the 1 σ uncertainty on each component of the motion. (a) Knot D. (b) Knot A. (c) Knots A and B.

BIRETTA, ZHOU, & OWEN (see 447, 588)

PLATE 28

A-E

A-M

A-W

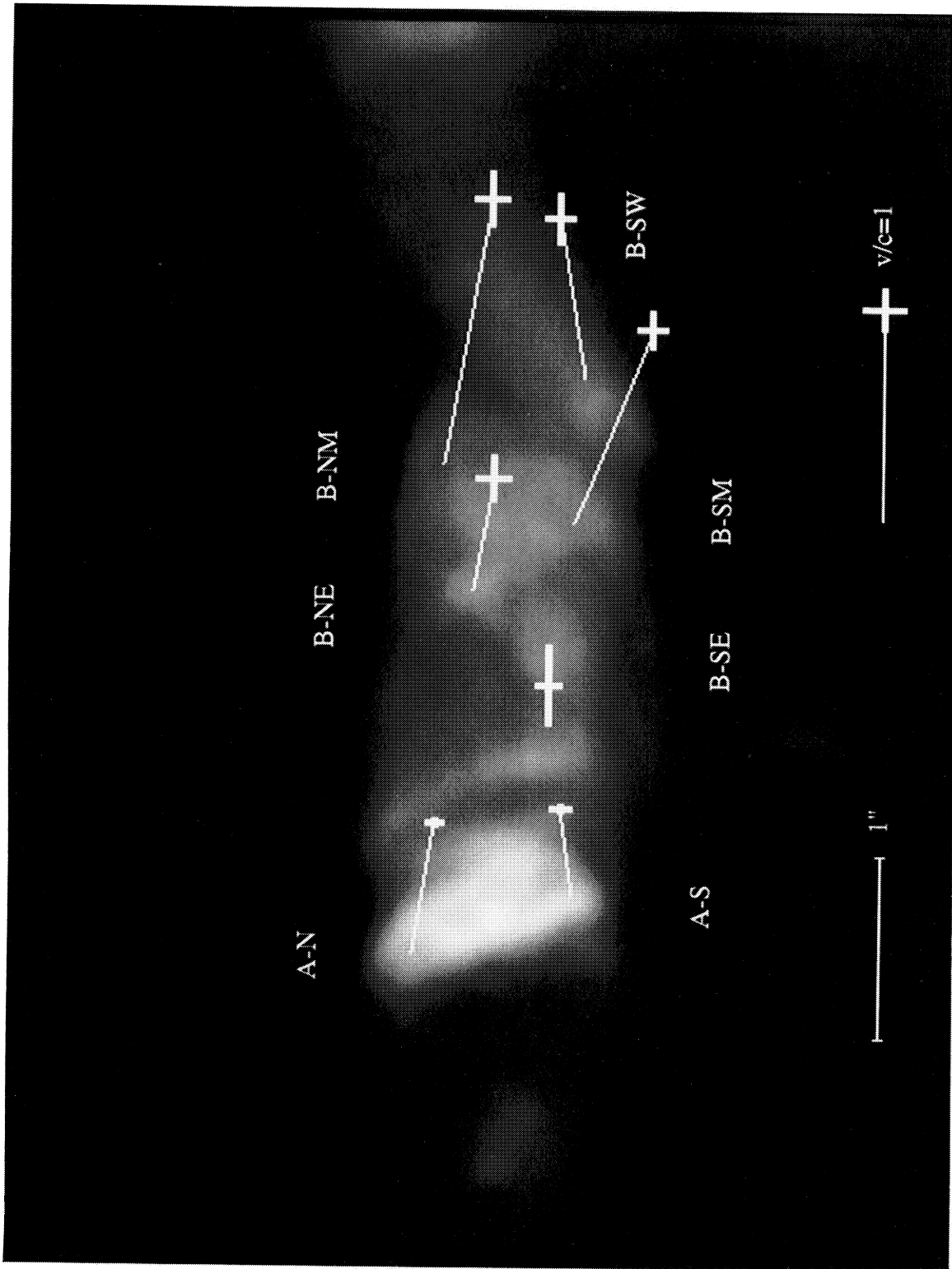v/c=1

1"

Fig. 7b

Biretta, Zhou, & Owen (see 447, 588)

PLATE 29

FIG. 7c

BIRETTA, ZHOU, & OWEN (see 447, 588)